LUND UNIVERSITY
Faculty of Science

# Diffusion MRI of Brain Tissue: Importance of Axonal Trajectory

Jan Brabec

Thesis submitted for the degree of Master of Science
Project duration: 9 months

Supervised by Markus Nilsson and Jan Pallon

MR Physics Group
Department of Physics
January 2018

# Abstract

Obtaining microstructural information non-invasively on brain tissue remains a challenge. Diffusion magnetic resonance imaging (dMRI) is an imaging method that can provide such information. That includes geometrical considerations of nerve cells projections, axons, that are present in the white matter of the human brain. Axons carry information encoded into electrical impulses to other cells.

The thesis deals with estimating parameters of the axonal trajectories, modeled as one-dimensional pathways, from the dMRI signal. That is achieved in two steps: constructing a forward model to predict the dMRI signal and, vice versa, estimating the tissue parameters from dMRI signal by solving the so-called inverse problem.

The proposed forward model employs a spectral analysis of dMRI signal. This formulation enables signal prediction for any gradient waveform and helps to identify the physical characteristics of the underlying system that are preserved in the dMRI signal. The physical properties are represented in so-called diffusion spectra whereas gradient waveforms, that sensitizes the signal, are in the encoding spectra.

To mimic biologically plausible axonal trajectories, axonal trajectories were modeled by a 1D-toy model that incorporates harmonic waves with variable degree of randomness. Different numerical methods for computation of diffusion spectra were compared, and the resulting spectra were characterized by a phenomenological model incorporating three parameters. It was not possible to estimate the exact parameters of the 1D-toy model from diffusion spectra. Nonetheless, it was possible to estimate their statistical descriptors, namely microscopic orientation dispersion and dispersion-weighted wavelength.

Solving the inverse problem posed a major challenge. The phenomenological model of the diffusion spectra was incorporated in a forward model of the diffusion-weighted signal perpendicular to the trajectory and applied to a state-of-the-art data acquired in human brain white matter of a healthy volunteer. It was not possible to estimate all the parameters of the phenomenological model but by constraining the parameters to plausible values we could estimate the last that was within the range predicted by histology. Incorporating trajectory-parameters in the model of white matter diffusion yielded fit residuals as small as those obtained with current state-of-the-art models assuming parallel, straight, and cylindrical cylinders. However, the cylinder model predicted axon diameters far outside the range expected from histology. We conclude that neglecting the axonal trajectories leads to biased models of axons in brain white matter.

# Popular Science

Magnetic resonance (MR) is a well-established modality that uses the nuclear magnetic resonance (NMR) phenomenon to probe magnetic properties of samples. MRI can serve as an example of successfully applied fundamental research from physics to biological sciences, humanities, chemistry or medicine. Biomolecules in biochemistry can be probed with atomic resolution. Nanomaterials in material sciences, porous rocks in geology, cell structures or tissues in biology and medicine can be examined. Statistical analysis of MRI signal can reveal functional state of the brain and is relevant in e.g. psychology. This thesis deals mainly with applications within medical sciences.

*Diffusion magnetic resonance imaging (dMRI)* unravels the tissue microstructure, i.e. the structure of tissue on the micrometer length scale. At this scale, the arrangement of cells and other biologically relevant structures emerges as a new property from a deeper, biochemical, scale. Microstructural appearance is often defining feature of biological tissues and is intertwined with their biological behavior, which is a highly interesting information from a medical point of view.

In this project, we study in a systematic way, often neglected, geometrical aspects of axons called *axonal trajectories*. Axons are the wiring of the brain. Based on microscopical images we proposed their representation, inspected their properties and forecasted the outcome of a diffusion measurement. The inverse question, whether the information on the axonal trajectories can be inferred from the outcome of measurement, and whether they could be neglected, was answered as well.

The results suggest that non-straight axonal trajectories need to be considered in the of representations of axons, although to estimate them reliably the practical diffusion measurements need to be improved. The estimated properties of axonal trajectories were congruent to the gold-standard method, microscopy.

Same methodology applied to the investigation of axonal trajectories can be employed in other problems in the dMRI field and may also lead to better understanding of the nature of the results of the diffusion measurements in the human tissue. Potentially, novel biomarkers that could help to diagnose diseases could be discovered. Generally, dMRI is an interesting research field where a potential breakthrough could be made. It probes the microstructural region that is highly important from the biological point of view, has a solid foundation in physical theory, allows for large variety of possible arrangements of the dMRI experiments and is not as widespread as other imaging modalities.

# Abbreviations and Acronyms

| | |
|---|---|
| 1D | One-Dimensional |
| 2D | Two-Dimensional |
| 3D | Three-Dimensional |
| ADC | Apparent Diffusion Coefficient |
| CSF | Cerebrospinal Fluid |
| CT | Computed Tomography |
| dMRI | Diffusion Magnetic Resonance Imaging |
| DTI | Diffusion Tensor Imaging |
| DWI | Diffusion Weighted Imaging |
| fMRI | Functional Magnetic Resonance Imaging |
| MCA | Middle Cerebral Artery |
| MR | Magnetic Resonance |
| MRI | Magnetic Resonance Imaging |
| NMR | Nuclear Magnetic Resonance |
| PET | Positron-Emission Tomography |
| RF | Radio-Frequency |
| SDE | Single Diffusion Encoding |
| SE | Spin-Echo |
| SSE | Sum of Square Differences Between the Measured Signal and the Predicted signal |
| μOD | Microscopic Orientation Dispersion |

# Contents

# Chapter 1

# Introduction

Medical imaging has become an indispensable tool in medical care. Its role is to reveal the internal structure of organisms, identify abnormalities and bolster informed decision-making based on their findings. Widespread medical imaging modalities include magnetic resonance imaging (MRI), positron emission tomography (PET), ultrasound, computed tomography (CT) or X-Ray imaging. Their working physical principles differ which means that their information content is different. However, they are complementary, probing the same object from a distinct perspective, adding a different piece to the puzzle. Magnetic resonance imaging is exceptional among them because it can be sensitized to a broad range of physical phenomena. That is why MRI should be, although included under a single term, more appropriately described as a collection of methods.

The thesis deals with the development of a biophysical model necessary for interpreting the results obtained from diffusion magnetic resonance imaging (dMRI) modality. The main application of dMRI is to non-invasively probe tissue microstructure, i.e. the structure of tissue on the micrometer length scale that is important from the biological point of view.

Diffusion magnetic resonance imaging measures the diffusional properties of water. If the diffusion takes place in a complex environment its geometry modulates the diffusional properties. Diffusion magnetic resonance signal thus contains indirectly the information on the geometrical properties by which is the diffusing water modulated.

The simplest and historically the first method applied in medical sciences with an important clinical impact is the measurement of Apparent Diffusion Coefficient (ADC; obtained by diffusion weighted imaging, DWI). Reduced ADC values are found the brain lesions affected by stroke, hence the ADC mapping is applicable in the stroke diagnostics [1]. Compared with the images obtained by Computed Tomography (CT) Angiography, the most widely used imaging technique used in stroke diagnostics, the changes in the brain structure are apparent earlier after the stroke onset (Fig. 1.1A)[2].

Another widely used method is the Diffusion Tensor Imaging (DTI)[3]. It estimates diffusivity along different directions which makes it suitable for studies of brain white matter which consists of elongated anisotropic tracts (bundles of nerve fibers)[4]. It is called tractography (Fig. 1.1B) and its applications are mainly focused in neurosciences, but the method has also been proven to be useful in pre-surgical planning [5].

Both ADC mapping and DTI, although commonly used, have drawbacks [7,8]. ADC, albeit sensitive, is not specific, which means it is often difficult to assign meaning to

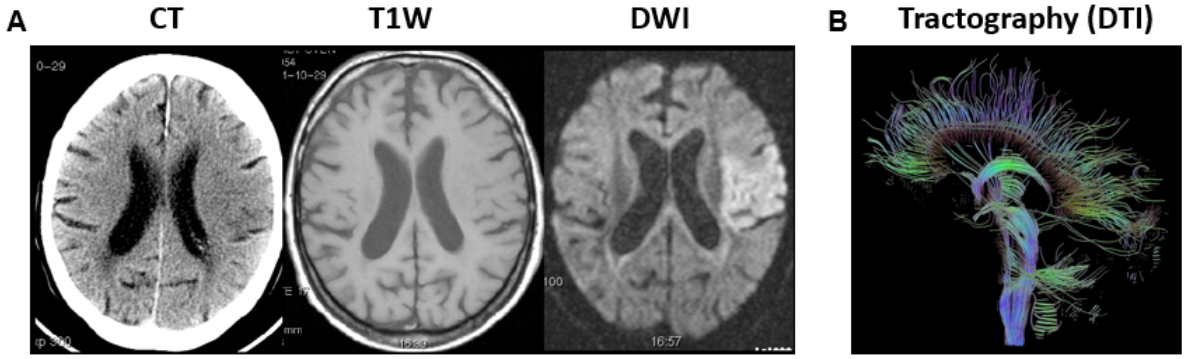


Figure 1.1: **Important clinical applications of dMRI. A: Stroke diagnostics.** Early stroke lesions are not detectable by CT or T1W modalities, but can be detected by diffusion-weighted imaging (DWI). Comparison between a CT image, T1-weighted MR image and (DWI) of the same patient within 2 hours after the stroke on-set. The lesion is depicted as a brighter (hyperintense) spot in the left hemisphere (on the right part of the image). It is most likely caused by an obstruction in the territory supplied by the middle cerebral artery (MCA). **B: Tractography using DTI.** The most apparent are tracts connecting the two hemispheres through corpus callosum and connecting the spine and brain. Source: [6].

changes in ADC values. That is also expressed in the name of the biomarker. The underlying biophysical quantity that ADC attempts to quantify is not well-defined, hence the adjective 'apparent'. Tractography based on DTI is confounded by other parameters such as orientation dispersion (misalignment) of axons [9]. Recent work indicates that it is not possible to reconstruct tracts even when the full knowledge of the underlying vector field is provided [10].

As a consequence, a more realistic model of diffusion of brain white matter that combined restricted and hindered diffusion, CHARMED, was applied to study human brain [11]. The era of connecting the physical diffusion properties with structural properties of axons began with a cylindrically restricted model of axons. The CHARMED was later extended, as AxCaliber, to include axon diameter distribution [12]. The axonal diameters could have been measured only in the perpendicular direction because the model was not invariant to the orientation of axons [13].

The potential usefulness of the axonal diameter estimate is that the higher axonal diameter is associated with a higher conduction velocity, whereas axons with smaller diameter can be more densely packed conveying information slowly but potentially more diverse in content [14]. Axons are, anatomically described, projections of neurons and, functionally, cables that convey information across different brain regions. Obstacles in the flow of information may manifest themselves in deterioration of cognitive abilities [15].

An orientationally invariant model estimating the axonal diameter that integrated the previous knowledge, ActiveAx, was proposed [16]. It offered the hope and hype that the diffusion properties and structural properties of axons can be connected in an easy and elegant way. However, the model has not met the expectations.

The diameter was found to be overestimated in the presence of axonal undulations and crossing fibers [17]. The effect was also investigated theoretically [18,19]. The importance of the extra-axonal space was not until recently realized [14]. Axons are not ideal cylinders

and it turns out that subtle folds of the axonal geometries have a significant impact on the signal [20].

A potential way forward may be the spectral analysis [21] and formulation of numerical forward models of complex geometries instead of relying on analytical predictions for simple ones. The formalism of the spectral analysis facilitates the formulation of the forward model (i.e. prediction of the signal from tissue parameters) for arbitrary gradient waveforms which can probe properties inaccessible by commonly used pulsed gradients [22]. That could facilitate the solution of the inverse problem. Numerical simulations of diffusion spectra are particularly useful to determine which properties of the underlying tissue can be, in principle, contained in the signal regardless of the experimental setup.

Unlike previous works, this project does not employ axonal diameter, but uses different axonal property, axonal trajectories represented by a 1D-toy model, to generate contrast in brain white matter. Axonal trajectories are the architecture of axons in the white matter of human brain. They are not simple but, on the contrary, rather complex and they are often described as undulating, i.e. having wavy- or harmonic course with a stochastic element. They can be observed in both intracranial and in extracranial nerves. Currently no unifying model of axonal trajectories exist, and it was not generally inspected which of the axonal trajectories properties are pertained in the dMRI signal. It is also not clear whether their properties can be estimated from the measured data of brain white matter in practice. To investigate the axonal trajectories independently, the axonal diameter was set to zero. The axonal undulations were characterized either as harmonic and represented by 1D harmonic waves parametrized by different amplitudes or as harmonic waves with a stochastic element parametrized by statistical descriptors.

Knowledge of axonal trajectories could be useful. It could serve as a non-invasive mapping of tissue mechanics. Undulating axons can stretch more and thus can withstand larger mechanical strains. That, in turn, can be useful in assessing recovery potential in e.g. hydrocephalus, a condition characterized by accumulation of cerebrospinal fluid in the brain, or in axon regeneration after peripheral nerve injury when extracranial nerves are damaged. The estimated axonal trajectories could be provided to the models that, due to the axonal undulations, overestimate the axonal diameter.

# Chapter 2

# Aims

The aim of the thesis is to answer research questions that are formulated below:

1. How can axonal trajectories be modeled?
2. How do the parameters of axonal trajectories translate into parameters of the diffusion spectra?
3. Are parameter estimates from models that assume straight cylinders biased by the presence of non-straight axonal trajectories?
4. Is it feasible to estimate diffusion spectra parameters in practice?
5. Is it feasible to estimate axonal trajectories parameters in practice?
6. Are the estimated trajectory parameters aligned with the predicted parameters obtained by the gold-standard methods?

# Chapter 3

# Background

The capabilities of every experimental technique – including magnetic resonance imaging - are fundamentally limited by their physical principles. This chapter outlines the basic concepts of magnetic resonance imaging (MRI) and basic principles of diffusion magnetic resonance imaging (dMRI). This chapter follows a bottom-up approach. Description of each method begins with a summary followed by the description of behavior of isolated system which later forms a distribution.

## 3.1 Principles of MR

The term 'magnetic resonance imaging' captures the key underlying physical principles of the MRI imaging modality. MRI probes magnetic properties (hence 'magnetic') facilitated by the interaction between nuclear spins and external magnetic field. The nuclear magnetic resonance phenomenon enables the measurement in practice (hence 'resonance'). The signal is localized and represented as an abstract object that reflects certain characteristics of the real object (hence 'imaging') [23–25].

The spins are excited by a magnetic field inside the bore that oscillates at the resonant frequency. In the near-field region produced by the coils the magnetic component of the electromagnetic field dominates[1] [26]. The dynamics of the resulting magnetic field created by the spins after the excitation is detected by the receiving coil and depends on the properties of the local spin environments within the sample.

Interaction with the external magnetic field is possible only when nuclear magnetic dipole moments $\mu$ are non-zero. That can attain only nuclei with non-zero nuclear spin[2] (more precisely total nuclear angular momentum). Quadrupole and higher moments are negligible. Non-zero nuclear spin is carried by nuclei whose total number of nucleons is odd since the individual angular momenta do not cancel out.

The human body consists mostly of water, $H_2O$. Hydrogen H has a spin of 1/2 and because it is the most abundant nucleus in human body, the highest sensitivity is

[1] In the literature, the excitation pulse is often described as a "radio-frequency pulse (RF)" or a "radio-wave". The term assumes both electronic and magnetic component. However, the near-field of MR scanner has much stronger magnetic component.

[2] Nuclear spin, or in other words total nuclear angular momentum, and nuclear magnetic moment have same direction but not magnitude. It would be clearer to refer to magnetic moments. However, it is more common in the MRI literature to refer to spins rather than to magnetic (dipole) moments.

achieved when the measurements reflect its properties. MRI thus studies properties of water. For example, its flow (perfusion MRI), distribution (structural MRI, most notably proton density sequences) or diffusion (diffusion MRI). However, hydrogen atoms are found in the human body not only as a part of water molecules. Some are constituents of saccharides, nucleotides, fats or proteins but their effect is in most practical MRI applications negligible. Concentrations of different nuclei, such as $^{15}$N or $^{13}$C, bound to specific structures can be the target of research that studies e.g. brain metabolite concentrations, part of MRI spectroscopy studies.

The behavior of the individual isolated spins is partly analogical to a classically behaving gyroscope, quantum mechanical aspects come into play. Unlike classically behaving objects with non-zero angular momentum (e.g. gyroscope), the individual isolated spins, when placed into the external magnetic field, B-field $\mathbf{B} = \mathrm{B}_0 \cdot \widehat{\mathbf{e_z}}$, can attain $2 \cdot \mathrm{I} + 1$ energy states, where I is the nuclear spin. The hydrogen is spin 1/2 particle and thus attain 2 states, referred to as spin-down and spin-up. Spins precess at Larmor frequency $\omega_0$:

$$\omega_0 = \gamma \cdot \mathrm{B}_0 \tag{3.1}$$

where $\gamma$ represents the gyromagnetic ratio [$\mathrm{rad} \cdot \mathrm{s}^{-1}\mathrm{T}^{-1}$], a ratio between nuclear magnetic moment and its angular momentum (hydrogen 42.6 MHz/T). The frequency is in radio-frequency range. The precession frequency is linear with the external magnetic field and is important both for signal acquisition and localization.

Individual spins form a spin distribution which is a bridging gap between nanoscale and macroscopic level. Macroscopically measurable quantity is the average over the spin distribution, the density of magnetic moments per volume, also called magnetization vector $\mathbf{M}$:

$$\mathbf{M} = \frac{1}{\mathrm{V}} \sum_{\text{all protons in V}} \boldsymbol{\mu} \tag{3.2}$$

The vector can be decomposed into transversal, $\mathbf{M}_{\mathrm{xy}} = \mathrm{M_x} \cdot \widehat{\mathbf{e}}_{\mathbf{x}} + \mathrm{M_y} \cdot \widehat{\mathbf{e}}_{\mathbf{y}}$, and longitudinal part, $\mathbf{M}_{\mathrm{z}} = \mathrm{M_z} \cdot \widehat{\mathbf{e}}_{\mathbf{z}}$, parallel to the external B-field; $\mathbf{M} = \mathbf{M}_{\mathrm{z}} + \mathbf{M}_{\mathrm{xy}}$. The macroscopic magnetization vector, unlike isolated quantum-mechanical objects, is a classically behaving vector that can attain any value.

The spin distribution obeys the thermodynamic principles. The potential energy associated with the magnetic field is $\mathrm{U_M} = -\mathbf{M} \cdot \mathbf{B}$ (i.e. $\mathrm{U} = -\boldsymbol{\mu} \cdot \mathbf{B}$ for individual spins). The energy is minimal when $\mathbf{M}$ and $\mathbf{B}$ are aligned. The spins are constantly tipped off by thermal energy leading to Boltzmann distribution (Fig. 3.1).

Magnetization $\mathbf{M}$ is not straightforwardly measurable in its equilibrium state. The spin excess along the external B-field is very small (roughly one in a million) due to the minuscule potential energy associated with the spin alignment compared to the thermal energy scale $\mathrm{k_B T}$. Magnetization $\mathbf{M}$ is thus masked by much stronger external magnetic field $\mathbf{B}_0$.

To detect the magnetization an extra radiofrequency (RF) pulse, or more precisely the left circularly polarized electromagnetic wave, is applied [26]. In the frame of reference that rotates at Larmor frequency, the RF pulse tips off the magnetization vector by a

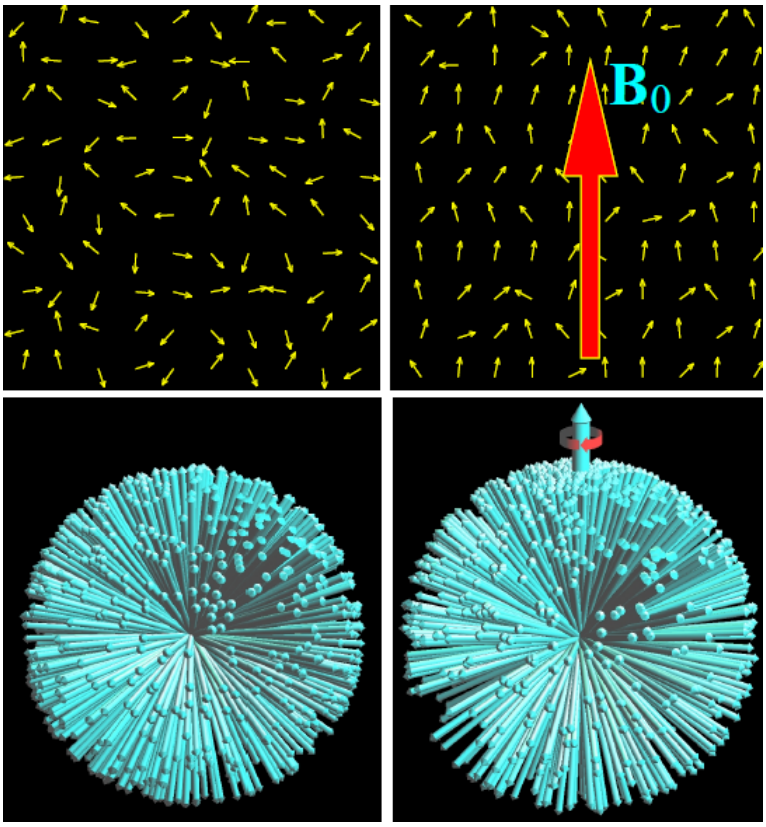


Figure 3.1: **Spin distributions.** The top row illustrates spin distribution in 2D before (top row, left column) and after (top row, right column) the external field is applied. The bottom row shows 3D spin distribution, respectively. Only a small fraction of spins is oriented along the external magnetic field due to relatively large thermal energy. The magnetization **M** (bottom row, right column; arrow pointing upward) is formed by averaging of the magnetic moments over the spin distribution. The whole distribution - and thus magnetization **M** – precesses around the external magnetic field. The precession itself is not detectable unless a radiofrequency (RF) pulse is applied. Source: *Hanson* [24].

flip angle 90° (Fig. 3.2). In the laboratory frame the trajectory corresponds to a circular motion. To tip off the vector effectively, the RF pulse must be applied at the 'resonance' (Larmor) frequency. Not all the RF field energy is used for spin flipping, some of it is absorbed by surrounding tissue in form of heat.

The dynamics of the magnetization vector gives rise to the measured signal. The magnetization vector that is in the equilibrium state aligned with the external magnetic field starts to precess perpendicularly to the field. The oscillatory magnetic field generated by the oscillating transverse magnetization $\mathbf{M}_{xy}$ induces voltage (Faraday's law) in the detector coils. The raw signal is recorded on detection coils and processed to obtain the final image. Some applications may use different flip angle than 90°.

Relaxation process governs the time-dynamics of the magnetization vector. The system reaches the original minimal energy configuration by dissipating energy in the form of heat. Two types of relaxation processes occur: a spin-lattice and a spin-spin relaxation.

Spin-lattice, or $T_1$, relaxation macroscopically corresponds to regrowth of longitudinal

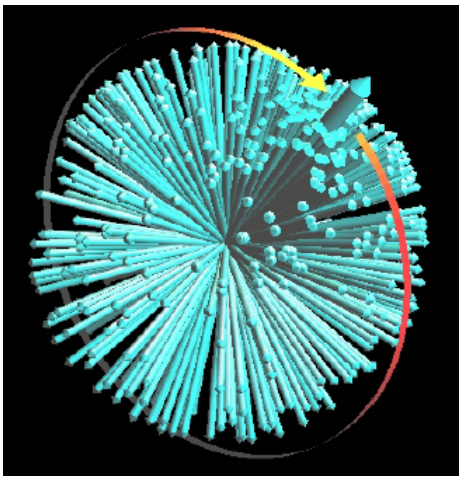

Figure 3.2: **Excitation.** Radiofrequency (RF) pulse flips the spin distribution by a certain degree as seen from a rotating frame of reference. The distribution can be characterized by magnetization $\mathbf{M}$ that is formed by averaging over the spin distribution. The whole distribution - as well as magnetization $\mathbf{M}$ - precesses around external magnetic field $\mathbf{B}_0$. Relaxation further occurs. *Hanson* [24].

magnetization $\mathbf{M}_z$. Spins are in thermal contact with the lattice that is composed of neighboring atoms. Exchange of energy between the spins and the lattice is the cause of the relaxation. Regrowth of $\mathbf{M}_z$ is exponential in time and characterized by the $T_1$ relaxation constant.

Spin-spin, or $T_2$, relaxation macroscopically corresponds to the reduction of the transverse magnetization $\mathbf{M}_{xy}$. The spins are influenced not only by the external magnetic field but also by the local non-homogeneous magnetic field produced by the surrounding spins. Local non-homogeneity is associated with different Larmor frequencies which, in turn, leads to dephasing ('directional randomizing') of the spins. That is reflected in the decrease of transversal magnetization $\mathbf{M}_{xy}$. The process is exponential in time and characterized by the $T_2$ relaxation constant.

In practice, the magnetic field $\mathbf{B}_0$ is not perfectly homogeneous which leads to an extra spin-spin dephasing characterized by the $T_2'$ relaxation constant. Nonetheless, it can be accounted for the inhomogeneities by a special pulse sequence design. The total relaxation constant due to the spin dephasing is given by: $1/T_2^* = 1/T_2 + 1/T_2'$. $T_2^*$ time is also relevant, for example one of the T2*-sensitive sequences are functional MRI (fMRI) sequences that reflect changes in ratio between oxygenated and deoxygenated hemoglobin and thus regional brain activation.

Both $T_1$ and $T_2$ constants are important and reflect different tissue characteristics. They are both widely used in the clinical applications. The rate at which transverse magnetization decrease is not same as the regrowth of longitudinal magnetization. In fact, $T_2$ and $T_1$ relaxation constants dramatically differ and carry different information [23].

MRI is an instrument with its fundamental limitations and application possibilities. The theory that explains the magnetic resonance signal originating from clinical scanners is an effective theory that identifies all the necessary parameters needed for explanation of experimental results. In the case of *clinical* MRI scanners, the macroscopic observable

is classically-behaving magnetization $\mathbf{M}$ and theory that explains its time evolution is a classical limit of a many-body quantum mechanical description. Bloch equation (Eq. 3.3) describes the time evolution of magnetization:

$$\frac{\mathrm{d}\mathbf{M}}{\mathrm{dt}} = \gamma\mathbf{M} \times \mathbf{B}_0 + \frac{1}{\mathrm{T}_1}(\mathbf{M}_0 - \mathbf{M}_\mathrm{z}) \cdot \widehat{\mathbf{e}_\mathbf{z}} - \frac{1}{\mathrm{T}_2}\mathbf{M}_\mathrm{xy} \tag{3.3}$$

All variables and parameters in the Eq. 3.3 were already introduced above. The Eq. 3.3 can be decomposed into three differential equations each describing behavior of $\mathbf{M}$ along a cartesian unit vector, $\mathbf{M}_\mathrm{z}$, $\mathbf{M}_\mathrm{x}$ and $\mathbf{M}_\mathrm{y}$, for derivation see [23]. However, the knowledge of quantum mechanical aspects is still important for understanding of the underlying processes and even more crucial in many other applications.

## 3.2 Imaging principles

Spatial variations in the properties of the magnetization vector carry information. The first step in the image reconstruction is to determine the signal at every volume element (voxel). The raw signal, as received by the receiving coils, originates from the whole body. The imaging principles of MRI radically differ from diffraction limited modalities, such as computed tomography or positron emission tomography, that directly localize the sources of radiation or attenuation. This approach is in MR not feasible since the raw signal has wavelength in radio-frequency range, i.e. order of meters.

The signal is processed in a reciprocal space termed k-space. The signal can be treated as a continuous quantity $\mathrm{S}(\mathbf{k})$ which is a Fourier Transform of spatial image intensity $\mathbf{I}(\mathbf{r})$:

$$\mathrm{S}(\mathbf{k}) = \mathscr{F}\{\mathrm{I}(\mathbf{r})\} = \int \mathrm{I}(\mathbf{r})\, \mathrm{e}^{-2\pi \mathrm{i}\, \mathbf{r}\cdot\mathbf{k}}\, \mathrm{d}\mathbf{r} \tag{3.4}$$

Wave-vector $\mathbf{k}$ is defined as:

$$\mathbf{k} = \frac{\gamma}{2\pi} \int \mathbf{g}(\mathrm{t})\, \mathrm{dt} \tag{3.5}$$

where $\gamma$ is the gyromagnetic ratio and $\mathbf{g}(\mathrm{t})$ gradient. Image intensity $\mathrm{I}(\mathbf{r})$ is obtained from the signal by the inverse Fourier Transform:

$$\mathrm{I}(\mathbf{r}) = \mathscr{F}^{-1}\{\mathrm{S}(\mathbf{k})\} = \int \mathrm{S}(\mathbf{k})\, \mathrm{e}^{2\pi \mathrm{i}\, \mathbf{r}\cdot\mathbf{k}}\, \mathrm{d}\mathbf{k} \tag{3.6}$$

Different gradients define different trajectories in k-space and determine how the k-space is filled out.

## 3.3 Physics of diffusion

The diffusion is defined as a net movement of particles from higher concentration to lower in the direction specified by the concentration gradient. However, so-called self-diffusion

takes place also in the absence of concentration gradient, due to the thermal (Brownian) motion. The distinction between the thermal motion and macroscopic diffusion smears out in diffusion MRI. The spins diffuse thermally but they are 'labeled' by diffusion sensitizing gradients according to their spatial location. The 'labeling' can be interpreted as a higher concentration of a distinct type of particles.

### 3.3.1 Fick's laws

Perhaps surprisingly, extremely complex physical processes including diffusion can be described by simple differential equations. The two differential equations that macroscopically describe diffusion are termed Fick's laws.

#### First Fick's law

The first Fick's law (Eq. 3.7) relates the molecular flux density $\mathbf{J}$ [$1/m^2s$] with concentration [$1/m^3$] gradient $\nabla$ through a diffusion tensor $\mathbf{D}$ [$m^2/s$]:

$$\mathbf{J}(\mathbf{r}, t) = -\mathbf{D}\nabla\mathbf{C}(\mathbf{r}, t) \tag{3.7}$$

The law states that molecular flux density $\mathbf{J}$ is proportional to concentration gradient $\nabla\mathbf{C}$ with the proportionality coefficient called the diffusion tensor $\mathbf{D}$. The tensor $\mathbf{D}$ has the form:

$$\mathbf{D} = \begin{pmatrix} D_{xx} & D_{xy} & D_{xz} \\ D_{yz} & D_{yy} & D_{yz} \\ D_{zx} & D_{zy} & D_{zz} \end{pmatrix} \tag{3.8}$$

where $D_{ij}, i \neq j$, are diffusion coefficients describing diffusion along a specific direction in the Cartesian coordinate system and $D_{ij}, i \neq j$, are correlation of motions between the individual directions. The diffusion tensor $\mathbf{D}$ is assumed to be symmetric, i.e. $D_{ij} = D_{ji}, \forall D_{ij}$, and thus only 6 independent values are needed to describe it. In its eigensystem, the diffusion tensor $\mathbf{D}$ (Eq. 3.8) can also be parametrized as:

$$\mathbf{D} = D_{iso}\left\{\begin{pmatrix} 1 & 0 & 0 \\ 0 & 1 & 0 \\ 0 & 0 & 1 \end{pmatrix} + D_{\Delta}\left[\begin{pmatrix} -1 & 0 & 0 \\ 0 & -1 & 0 \\ 0 & 0 & 2 \end{pmatrix} + D_{\eta}\begin{pmatrix} -1 & 0 & 0 \\ 0 & -1 & 0 \\ 0 & 0 & 0 \end{pmatrix}\right]\right\} \tag{3.9}$$

where $D_{iso}$ is the isotropic diffusivity, $D_{\Delta}$ is the normalized anisotropy, and $D_{\eta}$ is the asymmetry [27,28]. Throughout this text $D_{\eta} = 0$ is assumed. Although the data analysis is performed using the tensor formalism, for simplicity, we will further introduce, when useful, the concepts in 1 dimensions where the diffusion tensor $\mathbf{D}$ contracts to a tensor of order 0, i.e. to a scalar value, diffusion coefficient D.

**Second Fick's law**

The second Fick's law, that describes time evolution of concentrations, can be derived by considering the conservation of mass expressed in the continuity equation:

$$\begin{cases} \dfrac{\partial \mathbf{C}(\mathbf{r},\mathrm{t})}{\partial \mathrm{t}} = \vec{\nabla} \cdot (\mathbf{D}(\mathbf{r})\, \vec{\nabla}\mathbf{C}(\mathbf{r},\mathrm{t})) & \text{for } (\mathbf{r},\mathrm{t}) \in \bar{\mathbf{U}} \times \mathrm{t} \quad (3.10) \\ \mathbf{C}(\mathbf{r},\mathrm{t}) = \mathbf{f}(\mathbf{r},\mathrm{t}) & \text{for } (\mathbf{r},\mathrm{t}) \in \boldsymbol{\partial}\bar{\mathbf{U}} \times \mathrm{t} \quad (3.11) \\ \mathbf{C}(\mathbf{r},0) = \mathbf{g}(\mathbf{r}) & \text{for } (\mathbf{r},0) \in \bar{\mathbf{U}} \times 0 \quad (3.12) \end{cases}$$

where $\mathbf{C}(\mathbf{r},\mathrm{t})$ is concentration function at location $\mathbf{r}$ and time $\mathrm{t} \in [0,\infty)$, $\mathbf{U}$ domain of definition $\bar{\mathbf{U}}$ interior and $\boldsymbol{\partial}\mathbf{U}$ boundary, $\mathbf{D}(\mathbf{r})$ diffusion tensor at $\mathbf{r}$. Solution of the equation is a function $\mathbf{C} : \bar{\mathbf{U}} \times [0,\infty] \to \mathbb{R}$ that satisfies the above conditions [29].

The boundary condition $\mathbf{g}$ corresponds in-vivo to the geometry of the environment by which the diffusion is modulated. They influence the solution $\mathbf{C}$ and lies thus at the heart of the diffusion MRI. The initial condition $\mathbf{f}$ can be captured by a delta function and the total dMRI signal given by the average over all initial positions. Simplified, all the spins within the sample are 'labeled' according to their spatial position and the 'label' differs for different spatial positions.

### 3.3.2 Mean square displacement

Einstein realized that not only the concentration functions but also probability densities of particle displacements satisfy Fick's laws [30, 31]. That led to a natural explanation of macroscopic Fick's laws in terms of microscopical counterparts and offered a new paradigm of understanding diffusion.

Let us define a conditional probability density $\mathbf{P}$, called propagator, of finding a particle at position $\mathbf{r}$ after a diffusion time $\mathrm{t_d}$ given it was before at position $\mathbf{r}_0$, $\mathbf{P}(\mathbf{r}|\mathbf{r}_0,\mathrm{t_d})$. Let us also define particle density at point $\mathbf{r}$ as $\rho(\mathbf{r})$. Integrating over all starting position defines the *average propagator* [32]:

$$\mathbf{P}(\mathbf{r}|\mathrm{t_d}) = \int \rho(\mathbf{r_0})\mathbf{P}(\mathbf{r}_1|\mathbf{r}_0,\mathrm{t_d})\,\mathrm{d}\mathbf{r}_0 \quad (3.13)$$

The average propagator obeys Fick's laws and, hence, one can obtain specific solution of propagator by plugging the average propagator (Eq. 3.13) into the second Fick's law. Starting from a simple assumption, that the probability densities are the same if the time was reversed, $\mathbf{P}(\mathbf{r}|\mathrm{t_d}) = \mathbf{P}(\mathbf{r}|-\mathrm{t_d})$ Einstein derived the second Fick's law [30].

The boundary and initial conditions are crucial. If the space is infinite and homogeneous without any obstacles and all the particles initially are located at a single point, i.e. $\mathbf{g} = \boldsymbol{\delta}(\mathbf{r}–\mathbf{r_0})$ the solution becomes a Gaussian probability density centered at $\mathbf{r_0}$:

$$\mathbf{P}(\mathbf{r}|\mathrm{t_d}) = (4\pi\mathbf{D}\mathrm{t_d})^{-3/2}\, \mathrm{e}^{-\frac{(\mathbf{r}-\mathbf{r}_0)^2}{4\mathbf{D}\mathrm{t_d}}} \quad (3.14)$$

Deviation from the Gaussian shape can be a sign of hindrance or restriction of the geometry.

It is often useful to study only the variance of the propagator, termed mean square displacement, in different environments:

$$\mathbf{msd}^2(\mathrm{t_d}) = \langle(\mathbf{r}-\mathbf{r}_0)^2\rangle = \int_{\mathbb{R}^3}(\mathbf{r}-\mathbf{r}_0)^2\mathrm{P}(\mathbf{r}-\mathbf{r}_0|\mathrm{t_d})\,\mathrm{d}\mathbf{r}^3 \tag{3.15}$$

Conceptually, three different diffusion types can be defined: free, hindered and restricted diffusion (Fig. 3.3). Free diffusion is characterized by a compartment whose size is much larger than maximal mean square displacement whereas restricted by a compartment size that is smaller than mean square displacement. Hindered diffusion is characterized by a large compartment size but with obstacles present inside the compartment.


Figure 3.3: **Compartments.** **A**: free, **B**: hindered and **C**: restricted. Different compartments have significant effect on diffusion. Adapted from: *White* [33].

The mean square displacement of free diffusion is:

$$\mathbf{msd}^2(\mathrm{t_d}) = 6\mathbf{D}\mathrm{t_d} \tag{3.16}$$

and in 1D: $\mathrm{msd}^2(\mathrm{t_d}) = 2\mathrm{Dt_d}$.

The average apparent diffusion coefficient can be naturally defined from the mean square displacement as:

$$\mathrm{D(t)} \equiv \frac{\langle\Delta\mathrm{x}^2(\mathrm{t})\rangle}{2\mathrm{t}} \tag{3.17}$$

whereas the instantaneous diffusion coefficient can be defined as:

$$\mathrm{D_{inst}(t)} \equiv \frac{\partial}{\partial\mathrm{t}}\frac{\langle\Delta\mathrm{x}^2(\mathrm{t})\rangle}{2} \tag{3.18}$$

### 3.3.3 Time-dependent diffusion

Insight that the random walkers are the driving force of diffusion provides an intuition into time-dependent aspects of diffusion [34]. If the diffusion time is short the random walkers do not sense much of the geometry of the environment. When diffusion time is increased the walkers start to sense some of aspects of the environment. Ultimately, the walkers sense the whole environment and the diffusion coefficient reaches the limit

called tortuosity limit [35] but the information is less specific, as it contains all possible aspects what the walkers can sense. Since at different diffusion times a different degree of geometrical details is probed, the cross-over region can contain valuable information on the underlying geometry. Conceptually, the averaging of parameters as a function of diffusion time can be illustrated as blurring (Fig. 3.4).

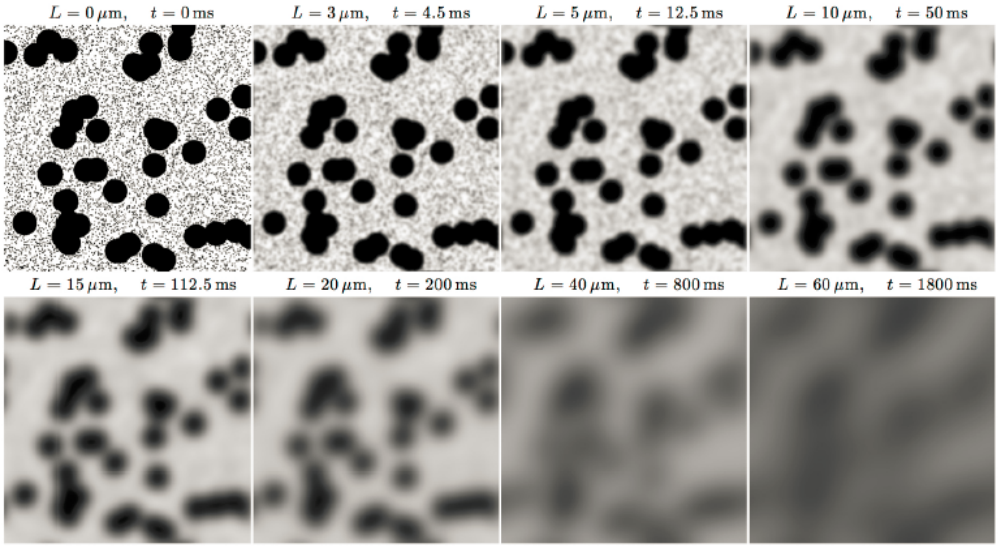


Figure 3.4: **Time-dependent diffusion as blurring.** Averaging of physical properties during the diffusion process on different diffusion-length and time-scales can be visualized as gradual smearing of the structural details. At short diffusion times, characteristics of the environment are contained in the spatially varying diffusion tensor $\mathbf{D}(\mathbf{r}, \mathrm{t})$. They are not, however, practically measurable. Longer diffusion times correspond to averaging of the local characteristics and ultimately merging $\mathbf{D}(\mathbf{r}, \mathrm{t})$ to a single diffusion tensor describing the whole voxel $\mathbf{D}(\mathrm{t} \to \infty)$. The goal is to find out how averaging $\mathbf{D}(\mathbf{r}, \mathrm{t})$ occurs in different environments at different diffusion times and which underlying characteristics of the underlying tissue are contained in the in the diffusion coefficient. Source: *Novikov* [35].

## 3.4 Measuring diffusion

### 3.4.1 Principles of dMRI

The fundamental equation of dMRI is the Bloch-Torrey equation (Eq. 3.19). As well as the Bloch equation (Eq. 3.3), Bloch-Torrey equation describes the evolution of magnetization $\mathbf{M}(\mathbf{r}, \mathrm{t})$ but in the presence of diffusion captured by the last term:

$$\frac{\mathrm{d}\mathbf{M}}{\mathrm{dt}} = \gamma \mathbf{M} \times \mathbf{B}_0 + \frac{1}{\mathrm{T}_1}(\mathbf{M}_0 - \mathbf{M}_\mathrm{z}) \cdot \widehat{\mathbf{e}_\mathbf{z}} - \frac{1}{\mathrm{T}_2}\mathbf{M}_\mathrm{xy} + \nabla \cdot \mathbf{D}\nabla\mathbf{M} \tag{3.19}$$

All the terms were already introduced in the description of Bloch equation (Eq. 3.3), the diffusion tensor $\mathbf{D}$ is introduced in the section Fick's law (Sec. 3.3.1).

Diffusion magnetic resonance imaging is an imaging modality whose signal represents a voxel-averaged Brownian motion of spin carrying nuclei. The dMRI signal is proportional to the average of transverse magnetization vector over a macroscopic voxel-volume:

$$\mathrm{S}[\mathrm{t}, \mathbf{g}(\mathrm{t})] \propto \int_{\mathrm{V}} \mathbf{M}_{\mathrm{xy}}(\mathbf{r}, \mathrm{t})\, \mathrm{d}\mathbf{r} \tag{3.20}$$

The signal originating from a physical volume is mapped onto a point termed voxel. Its physical volume is in the most clinical MR application measured in units of $\mathrm{mm}^3$. However, the relevant dimensions of tissue properties are in the units of $\mu\mathrm{m}^3$.

To obtain the microstructural information on the tissue beyond the nominal image resolution one needs to rely on biophysical modeling. The voxel is divided into sub-voxel regions, for example commonly into intra- and extra-cellular region, and the signal obtained on the voxel-level can be interpreted as a weighted mean of a statistical distribution of signals originating from different sub-voxel regions. Weights correspond to amount of spins in the sub-voxel regions or, more intuitively, to volume fractions. The regions may not be independent, they may exchange particles through e.g. channels embedded in cell membranes, which may complicate the interpretation.

### 3.4.2 dMRI sequences

Sequences of magnetic gradients encode information into the MR signal. Pulse sequences can be modified by adding diffusion gradients to become diffusion sensitive. They lead to additional dephasing given by:

$$\Phi(\mathrm{t}) = \int_0^{\mathrm{t}} \mathrm{g}(\mathrm{t}')\mathrm{x}(\mathrm{t}')\mathrm{d}\mathrm{t}' \tag{3.21}$$

where g(t) is the effective gradient [T/m] applied along a specific direction and x(t) is Brownian trajectory [m] along the direction of the diffusion gradient. Each spin contributes to the overall phase dispersion and the total signal is approximately given by the exponential decay of the average phase dispersion:

$$\mathrm{S} = \mathrm{e}^{-\langle \Phi(\mathrm{t})^2 \rangle} \tag{3.22}$$

#### Single diffusion encoding

The most commonly used diffusion gradients can be categorized as single diffusion encoding gradients (SDE) [36]. These consist of a single pair of encoding (dephasing) and decoding (rephasing) pulsed diffusion gradients. Historically the first and the most commonly employed diffusion encoding sequence in clinical applications is the Stejskal-Tanner Spin Echo Pulse Sequence [37]. Two symmetric diffusion gradients are added to a spin-echo (SE) sequence [23] (Fig. 3.5).

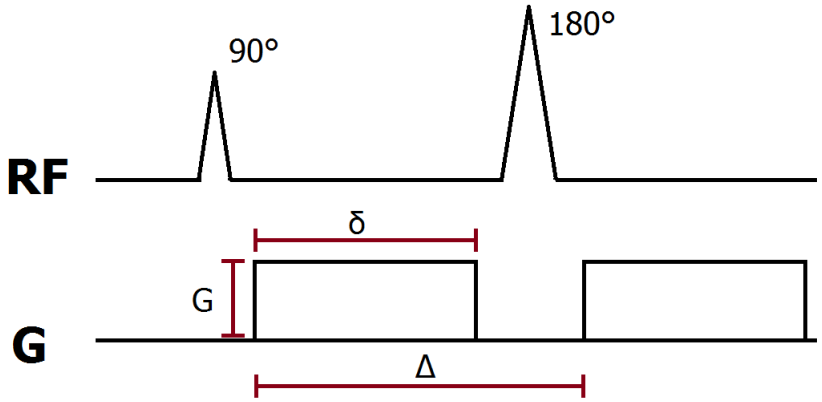


Figure 3.5: **Stejskal-Tanner Sequence.** Stejskal-Tanner Spin Echo Pulse Sequence is historically the first sequence that was designed to sensitize the signal to diffusion. It consists of two pulsed magnetic gradients placed between two RF pulses and defined by 3 parameters: G [T/m] is the gradient strength, $\delta$ [s] and $\Delta$ [s] encoding and diffusion times, respectively.

The signal S follows a mono-exponential decay provided that the diffusion is free. The exponent depends on the parameters of the sequence as well as on the diffusion coefficient:

$$\frac{S}{S_0} = e^{-bD} \tag{3.23}$$

$S_0$ refers to the signal measured in the absence of the diffusion sensitizing gradients, i.e. $b = 0$. A measure of diffusion encoding strength is called b-value and is derived for Stejskal-Tanner sequence:

$$b = \gamma^2 G^2 \delta^2 t_d = \gamma^2 G^2 \delta^2 (\Delta - \frac{1}{3}\delta) \tag{3.24}$$

where G [T/m]is gradient strength, $\delta$ [s] and $\Delta$ [s] are encoding and diffusion times, respectively, and $t_d = \Delta - \delta/3$ is referred to as the effective diffusion time.

In practice, the diffusion coefficient D is the unknown. The b-value is specified by experimental setup, signal S and background signal $S_0$ are obtained from the measurement. Hence, the diffusion coefficient D can be obtained by fitting Eq. 3.23 to an experimentally obtained signal-versus-b-curve.

The b-value is to be understood as a bare abbreviation or as a collective label for the 'defining' parameters given in the Eq. 3.24 because substantial impact on the signal has also the choice of diffusion times.

# Chapter 4

# Theory

Now we introduce the tools needed to understand the analysis part. The spectral formulation is introduced together with theoretical analysis of the diffusion spectra in various geometries. Axonal trajectories are studied from the microscopical point of view.

## 4.1 Diffusion spectrum

The ideas laid down in the section on time-dependent diffusion (Sec. 3.3.3) can be brought further from a different perspective. If any obstacles in the compartment are present, then the velocities of the diffusing particles will become correlated. In other words, the autocorrelation function exhibits a pattern related to the compartment geometry.

### 4.1.1 Velocity autocorrelation function

The properties of stochastic variables can be studied through their autocorrelation functions [38]. Given measurements $\mathrm{v}_1, \mathrm{v}_2, ...\mathrm{v}_\mathrm{N}$, the lag $\tau$ autocorrelation function is defined as:

$$\mathrm{R(t)} = \frac{\mathrm{E}[(\mathrm{v}_{\mathrm{t}_0} - \bar{\mathrm{v}})(\mathrm{v}_{\mathrm{t}_0+\tau} - \bar{\mathrm{v}})]}{\sigma^2} \tag{4.1}$$

Provided the diffusion time is small enough, particles can move in any direction with equal probability, and thus the mean velocity is $\bar{\mathrm{v}} = 0$. Provided the statistical properties do not change over time (for example, the geometry of the compartment cannot change or particles cannot escape) and the time-series is ergodic (i.e. statistical properties are deducible from a sufficiently long time-series; for example, the particles must sense a representative sample of the compartment geometry) the expected value (Eq. 4.1) can be estimated by an average:

$$\mathrm{R(t)} \approx \frac{\langle\langle \mathrm{v}(\mathrm{t}_0)\mathrm{v}(\mathrm{t})\rangle\rangle}{\sigma^2} \tag{4.2}$$

where the inner brackets $\langle\cdot\rangle$ represent an arithmetic average over the diffusing particles and the outer brackets $\langle\cdot\rangle$ over all possible starting positions. Instead of double brackets

we will write only single brackets.

Diffusion spectrum [21] is defined as a Fourier transform of velocity autocorrelation function (Eq. 4.1):

$$\mathrm{D}(\omega) = \mathscr{F}\{\langle \mathrm{v}(\mathrm{t}_0)\mathrm{v}(\mathrm{t})\rangle\} \tag{4.3}$$

The velocity autocorrelation function, mean square displacement and diffusion spectrum contain the same information since these three quantities are related according to:

$$\langle \Delta \mathrm{x}^2(\mathrm{t})\rangle = 2\int_0^{\mathrm{t}'}\int_0^{\mathrm{t}''} \chi(\mathrm{t}')\mathrm{d}\mathrm{t}'\mathrm{d}\mathrm{t}'' = \frac{4}{\pi}\int_0^{\infty} \frac{\mathrm{D}(\omega)}{\omega^2}[1-\cos(\omega \mathrm{t})]\mathrm{d}\omega \tag{4.4}$$

## 4.2 Encoding spectrum

It is useful to consider a spectrum of an encoding waveform, *q-vector*:

$$\mathrm{q}(\mathrm{t}) = \gamma \int_0^{\tau} \mathrm{g}(\mathrm{t}')\,\mathrm{d}\mathrm{t}' \tag{4.5}$$

where $\tau$ is the time between the beginning of the diffusion sensitizing gradient and the echo, called echo-time. The q-vector can be studied in the frequency domain by considering its Fourier transform:

$$\mathrm{q}(\omega) = \mathscr{F}\{\mathrm{q}(\mathrm{t})\} = \int \mathrm{q}(\mathrm{t})\,\mathrm{e}^{-2\pi \mathrm{i}\,\mathrm{t}\cdot\omega}\,\mathrm{d}\mathrm{t} \tag{4.6}$$

We refer to the power spectrum as the *encoding spectrum*:

$$|\mathrm{q}(\omega)|^2 \tag{4.7}$$

b-value from the encoding spectrum can be obtained as an integral over all frequencies:

$$\mathrm{b} = \int |\mathrm{q}(\omega)|^2\,\mathrm{d}\omega \tag{4.8}$$

## 4.3 Signal in spectral formulation

Signal within the spectral formulation is given by the integral over the diffusion spectrum weighted by the encoding spectrum at each frequency [21]:

$$\mathrm{S} = \mathrm{e}^{-\int \mathrm{D}(\omega)\cdot|\mathrm{q}(\omega)|^2\mathrm{d}\omega} \tag{4.9}$$

The expression (Eq. 4.9) is only approximate since it is derived as a first cumulant expansion of the signal [21]. The operation in the exponent determines which part of the diffusion spectra is contained in the signal (Fig. 4.1).

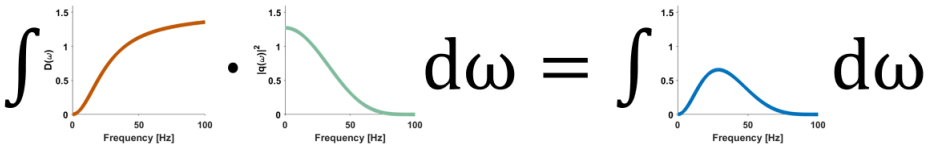


Figure 4.1: **Weighting of the diffusion spectrum by encoding spectrum.** The encoding spectrum (green curve; middle) determines which part of the diffusion spectrum (red curve; left) is pertained in the signal. The function that is integrated is depicted as yellow curve (right). The units are chosen arbitrarily.

## 4.4 Diffusion spectrum in different geometries

### 4.4.1 Free diffusion (1D)

The diffusion spectrum is a constant (derivation is shown in the Appendix 10):

$$\mathrm{D}(\omega) = \mathrm{D} \tag{4.10}$$

### 4.4.2 Restricted diffusion in simple geometries (1D, 2D, 3D)

Diffusion spectra can be derived for planar, cylindrical and spherical geometries analytically (Appendix 10).

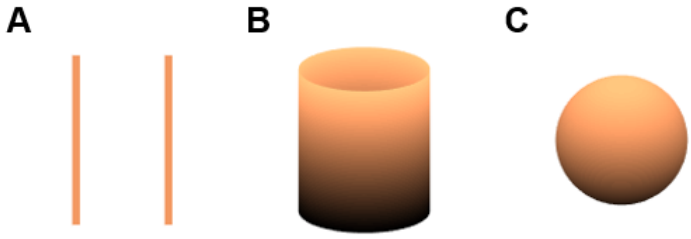


Figure 4.2: **Simple Geometries.** Analytical expressions of diffusion spectra for simple geometries are available in the literature [21,39]. **A**: planar, **B**: cylindrical, **C**: spherical.

### 4.4.3 Restricted and hindered diffusion in harmonic waves (1D×1D)

A harmonic wave of diameter 0, parametrized by its amplitude A and wavelength $\lambda$, is given by:

$$\mathrm{y(x)} = \mathrm{A} \cdot \sin(\Phi) = \mathrm{A} \cdot \sin\left(2\pi \cdot \frac{\mathrm{x}}{\lambda}\right) \tag{4.11}$$

Where $\Phi$ is referred to as phase.

From this location the actual investigation performed by the student begins. We will study the limiting behavior at short- and long-diffusion times parallel (hindered diffusion) and perpendicular (restricted diffusion) to the path of the wave theoretically and the half-width half maximum of the cross-over regime between the long- and short-diffusion times in the perpendicular direction.

The diffusion is restricted in y-direction within the interval [–A; A]. On the other hand, diffusion parallel to the propagation is hindered since it does not have a lower and upper bound.

### Short-diffusion times

At short diffusion times, $t \to 0$, the random walkers do not sense the curvature of the trajectory but behave as if they diffused in straight but angulated subsegments (Fig. 4.3A). *Perpendicular diffusion coefficient*, $D_\perp$, at position $x_0$ is thus:

$$D_\perp(x_0, t \to 0) = \frac{(\sin(x_0) \cdot \Delta\mathbf{r})^2}{\Delta t} = \sin^2(x_0) \cdot \frac{\Delta\mathbf{r}^2}{\Delta t} = \sin^2(x_0) \cdot D_0 \tag{4.12}$$

Where $D_0$ is referred to as bulk diffusion coefficient, i.e. free diffusion coefficient. Averaging over all walkers' initial positions yield a diffusion coefficient that has lower value than the bulk diffusion coefficient:

$$D_\perp(t \to 0) = \frac{1}{||x_0||} \int_{x_0} \sin^2(\Theta(x_0)) \cdot D_0 \, dx_0 = \langle \sin^2(\Theta(x_0)) \rangle \cdot D_0 = \tag{4.13}$$

$$= \langle \mu OD_\perp(x_0) \rangle \cdot D_0 = \mu OD_\perp \cdot D_0 \tag{4.14}$$

We refer to the value $\sin^2(\Theta(x_0))$ as microscopic orientation dispersion, $\mu OD_\perp$. In the case of sine waves it is given by:

$$\mu OD_\perp = \langle \mu OD_\perp(x_0) \rangle = \langle \sin^2(\Theta(x_0)) \rangle = \left\langle \left( \tan^{-1} \left( \frac{d}{dx} y(x) \right) \right)^2 \right\rangle \tag{4.15}$$

The diffusion coefficient in the *parallel* direction, $D_\parallel$, is given by the similar equation but the sine is replaced by a cosine function:

$$D_\parallel(t \to 0) = \langle \cos^2(\Theta(x_0)) \rangle \cdot D_0 = \mu OD_\parallel \cdot D_0 \tag{4.16}$$

### Long-diffusion times

At very long diffusion times, $t \to \infty$, the random walkers probe all trajectories and behave as if they diffused along a straight line (Fig. 4.3A).

In the *perpendicular* direction the diffusion is restricted and thus the perpendicular mean square displacement at very long diffusion times becomes almost constant. Derivative of a constant value with respect to the time is zero and thus the diffusion coefficient becomes:

$$\mathrm{D}_{\perp}(\mathrm{t} \to \infty) = 0 \tag{4.17}$$

From now on we will drop the subscript "$\perp$" because all further analysis was performed perpendicular to the direction of propagation. In the *parallel* direction the walkers longer time $\tau > \mathrm{t}$ to reach the same distance as compared to a diffusion on a straight line. The diffusion coefficient is smaller:

$$\mathrm{D}_{\parallel;\,\mathrm{sine}}(\mathrm{t} \to \infty) = \frac{\Delta \mathrm{x}^2}{\Delta \tau} = \frac{\Delta \mathrm{x}^2}{\Delta(\mathrm{ct})} = \frac{1}{\mathrm{c}(\mathrm{A}, \lambda)} \mathrm{D}_{\mathrm{line}}(\mathrm{t} \to \infty) < \mathrm{D}_{\mathrm{line}} \tag{4.18}$$

where $1/\mathrm{c}(\mathrm{A}, \lambda) < 1$ is a constant, referred to as the tortuosity limit, and proportional to the ratio of the length of the curve the walkers need to traverse and length of the straight line:

$$\mathrm{c}(\mathrm{A}, \lambda) \propto \frac{\int_{\mathrm{C}} \mathrm{y}(\mathrm{x})\, \mathrm{ds}}{||\mathrm{x}||} \tag{4.19}$$

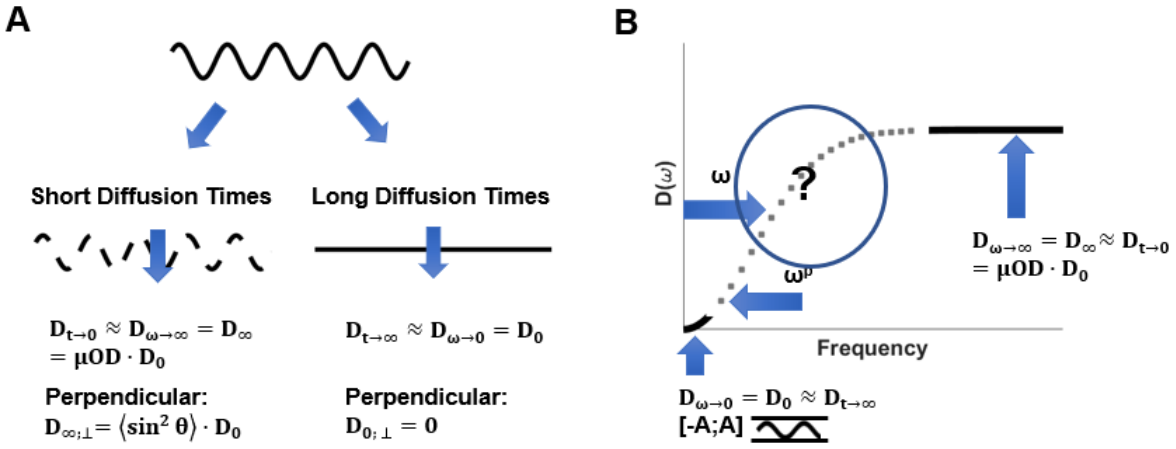


Figure 4.3: **Diffusion in harmonic waves, perpendicular direction. A:** In the short-time regime, the walkers do not sense the curvature of the environment but move in straight but orientationally dispersed sub-segments. In the long-time regime, the characteristics of the environment is averaged out as if the walkers moved in a straight wire. **B: Diffusion spectrum.** In the short-time regime, the diffusion spectrum is given by the orientation dispersion. On the other hand, in the long-time regime, since the walkers probe the whole structure, the geometry of a harmonic wave is "averaged out" and the diffusion spectrum is similar to a diffusion between two planes. The intermediate regime is of interest as well. It may be characterized by the spectral width $\omega$, i.e. the half-width half maximum.

### Half-width half maximum $\omega$ in the perpendicular direction

If wavelength $\lambda \to \infty$ the displacement in the perpendicular direction is not zero and, oppositely, if $\lambda \to 0$ the diffusion becomes in the perpendicular direction free.

We hypothesize that the diffusion coefficient is proportional to an "average" wavelength that is weighted by the local microscopic orientation dispersion $\mu\mathrm{OD}(\mathrm{x}_0)$ and normalized to the averaged $\mu$OD (Fig. 4.4). We define the dispersion-weighted wavelength as:

$$\lambda_\sigma = \left( \frac{\langle \mu\mathrm{OD}(\mathrm{x}_0) \cdot \lambda^{-1}(\mathrm{x}_0) \rangle}{\mu\mathrm{OD}} \right)^{-1} \tag{4.20}$$

where the 'local' wavenumber is $\lambda^{-1}(\mathrm{x}) = \mathrm{d}/\mathrm{dx}\,\Phi(\mathrm{x})$, in the case of sine waves $\lambda^{-1}(\mathrm{x}) = \lambda^{-1}$. Based on the dimensional analysis we find that:

$$\omega = \lambda_\sigma^{-2} \cdot \mathrm{D}_0 = \left( \frac{\langle \mu\mathrm{OD}(\mathrm{x}_0) \cdot \lambda^{-1}(\mathrm{x}_0) \rangle}{\mu\mathrm{OD}} \right)^{-2} \cdot \mathrm{D}_0 \tag{4.21}$$

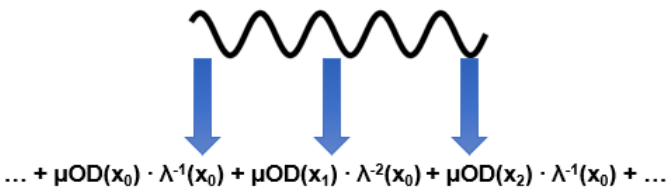


Figure 4.4: **Dispersion-weighted wavelength.** A local wavenumber $\lambda^{-1}(\mathrm{x}_0)$ is weighted by a local microscopic orientation dispersion $\mu\mathrm{OD}(\mathrm{x}_0)$. All wavenumbers $\lambda^{-1}(\mathrm{x}_0)$ are averaged and normalized to the average microscopical orientation dispersion $\mu$OD. A local wavenumber $\lambda^{-1}(\mathrm{x}_0)$ in the case of a sine wave is equal to the inverse of the wavelength: $\lambda^{-1}(\mathrm{x}_0) = \lambda^{-1}$.

### 4.4.4 Biology of axonal trajectories

The axonal trajectories of optic nerve (cranial nerve; Fig. 4.5A), corpus callosum (bundle of fibers connecting left and right hemisphere; Fig. 4.5B) and phrenic nerve (extra-cranial nerve; Fig. 4.5C) bear similar undulations patterns. The general characteristic could be captured by harmonic waves with variable amplitude a and wavelength $\lambda$ (Tab. 4.1).

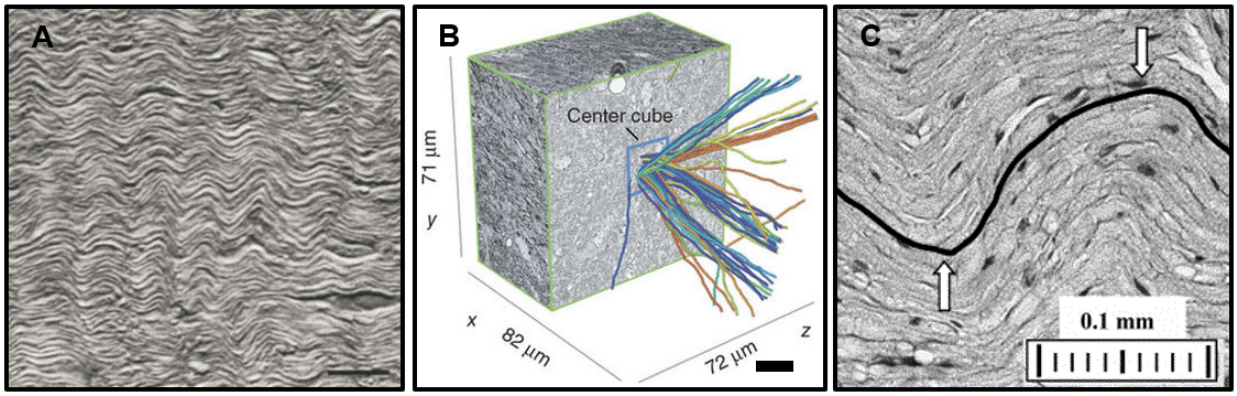


Figure 4.5: **Optic nerve, corpus callosum and phrenic nerve. A:** Optic nerve of a rat obtained by microscopy exhibits undulations. Scale bar = 20 µm. Source: [40]. **B:** Corpus callosum of a mouse obtained by electron microscopy with reconstructed 50 axonal trajectories. Source: [41] **C:** Fiber undulation in the longitudinal cross section of pig phrenic nerve. Scale bar = 0.1 mm. Source: [42].

Table 4.1: **Representation of axons as harmonic axonal trajectories.** Estimated values of amplitude, wavelength and mean axonal diameter of optic nerve [18, 40, 43], corpus callosum [17,41,44–49] and phrenic nerve [42,50]. The axonal diameter in corpus callosum shows rather a distribution of diameters ranging from 0.5 µm to 14 µm, the volume-weighted average is below 1 µm.

| | **Optic nerve** | **Corpus callosum** | **Phrenic nerve** |
|---|---|---|---|
| **Amplitude a** [µm] | 5 | 1 – 10 | 20 – 100 |
| **Wavelength** $\lambda$ [µm] | 20 – 30 | 10 – 35 | 100 – 500 |
| **Diameter d** [µm] | 1 | 0.5 | 4 – 5 |

# Chapter 5

# Estimating microstructural features by modeling

Biophysical models relate parameters of important aspects of biological tissues to outcomes of the experiment, to dMRI signal [51]. With such models in hand, the tissue parameters can be obtained from the dMRI signal by solving an inverse problem. The inverse problem is the problem we are facing when analyzing experiments. It is often ill-defined and poses a major challenge [52].

A common strategy how to circumvent the problem is to constrain the model and assume specific values of some parameters. However, the constraints may not be satisfied in practice and the results may lead to misinterpretations in situations where they do not apply.

To introduce a common strategy in the modeling, an *Open model*, that introduce the general features of the analyzed models, will be defined. Afterwards the specific assumptions of the analyzed models, ActiveAx and Axonal trajectory model, will be introduced into the *Open model*.

## 5.1 The Open model

This model is intended to illustrate key features, but was not be used in practice. It was created by identifying the common features of the analyzed model, ActiveAx and Axonal trajectory model, and serves for explanatory purposes. This model does not relate diffusional properties and tissue properties.

The *Open model* has 2 compartments, namely extra-cellular and intra-cellular, and the total signal is given by:

$$S = S_0 \left(f_{ic} \cdot S_{ic} + f_{ec} \cdot S_{ec}\right) = S_0 \left(f_{ic} \cdot S_{ic} + (1 - f_{ic}) \cdot S_{ec}\right) \tag{5.1}$$

Where $f_{ic}$ and $f_{ec}$ are spin fractions of the intra-axonal and extra-axonal space, respectively. Both intra- and extra-axonal signal, $S_{ic}$ and $S_{ec}$, by the equation of the same form:

$$\begin{cases} S_{ic} = e^{-[bD_{ic;\perp}(\mathbf{n}\cdot\mathbf{u})+bD_{ic;\parallel}(1-(\mathbf{u}\cdot\mathbf{n})^2)]} \\ S_{ec} = e^{-[bD_{ec;\perp}(\mathbf{n}\cdot\mathbf{u})+bD_{ec;\parallel}(1-(\mathbf{u}\cdot\mathbf{n})^2)]} \end{cases} \tag{5.2}$$

where $D_{ic;\parallel}$ and $D_{ec;\parallel}$ are intra- and extra-cellular axial diffusivities (parallel to the direction of the maximal diffusivity), intra- and extra-cellular radial (perpendicular) diffusivities, $D_{ic;\perp}$ and $D_{ec;\perp}$, respectively. $\mathbf{u}$ is the direction of the maximal diffusivity, $\mathbf{n}$ direction of measurement and "$\cdot$" depicts the inner product between two vectors.

The Open model explicitly employs five assumptions:

- Total signal S can be modeled as a sum of two independent signal fractions.
- Both extra- and intra-cellular signal attenuations are approximately mono-exponential.
- Intra- and extra-cellular diffusion tensors describe the intra- and extra-axonal spaces.
- A collection of experiments fully describes the experiment.
- No other factors contribute to the total signal.

The Open model contains 13 free parameters: $S_0$, $f_{ic}$, $f_{ec}$, 6 values needed to determine the direction of the two vectors, $\mathbf{n}$ and $\mathbf{u}$. The estimated free parameters are found by calculating the minimum of the square differences between predicted and estimated total signal (SSE).

## 5.2 ActiveAx

ActiveAx attempts to link diffusional properties to tissue properties, notably to the axonal diameter d [16].

Compared with the Open model, it adds two additional compartments: cerebrospinal fluid (CSF) and trapped water compartment (where the water cannot diffusive but is stationary). The total signal is given by the sum of signal fraction of the four compartments:

$$S = S_0 \sum_{i=1}^{4} f_i \cdot S_i \tag{5.3}$$

It models the intra-axonal compartment as parallel straight cylinders with equal diameter d where the intra-cellular radial diffusivity $D_{ic;\perp}$ is given by time-domain version of the analytical prediction formulated in frequency domain (Sec. 4.4.2).

Extra-axonal compartment is modeled in the same way as in the Open model but introduces three additional constraints. The extra-axonal axial diffusivity (i.e. parallel to the propagation of axons) $D_{ec;\parallel}$ is constrained to the same value as the intra-axonal intrinsic diffusivity $D_{ic;0}$ and as well as to the same value as axial diffusivity $D_{ic;\parallel}$. The extra-axonal axial diffusivity (parallel to the propagation of axons) $D_{ec;\perp}$ is constrained to the extra-axonal radial diffusivity $D_{ec;\parallel}$ by:

$$D_{ec;\perp} = D_{ec;\parallel}(1-\nu) \tag{5.4}$$

Where $\nu$ is called tortuosity given by:

$$\nu = \frac{\mathrm{f_{ic}}}{\mathrm{f_{ic}} + \mathrm{f_{ec}}} \tag{5.5}$$

The geometry of cerebrospinal fluid compartment is assumed to be isotropic, i.e. described by a diffusion tensor $\mathbf{D}_{\mathrm{CSV}}$ with $\mathrm{D_{iso}} > 0$ but $\mathrm{D}_\Delta = 0$. The trapped water compartment is assumed to be highly restricted meaning that the spins are almost stationary and do not diffuse, hence, $\mathrm{S}_4 = 1$.

The model contains in total 11 free parameters: $\mathrm{S}_0$, $\mathrm{f_{ic}}$, $\mathrm{f_{ec}}$, $\mathrm{f_{CSV}}$, $\mathrm{f_{trapped\,water}}$, $\mathrm{D_{ec;\parallel}}$, axonal diameter d and the axis of the cylinders $\mathbf{n}$.

## 5.3 Axonal trajectory model

This model attempts to link the diffusional properties to tissue properties, here to axonal trajectories, by introducing different constraints. The model builds on one of the best scoring model of the White matter modeling challenge [53], developed by the supervisor. The Open model is modified in the two ways:

Firstly, unlike the Open model and ActiveAx, it accounts for the $\mathrm{T}_2$ decay, hence intra- and extra-axonal signals, $\mathrm{S_{ic}}$, $\mathrm{S_{ec}}$, are given by:

$$\begin{cases} \mathrm{S_{ic}} = \mathrm{e}^{-[\mathrm{bD_{ic;\perp}}(\mathbf{n}\cdot\mathbf{u}) + \mathrm{bD_{ic;\parallel}}\,(1-(\mathbf{u}\cdot\mathbf{n})^2)]} \cdot \mathrm{e}^{-\mathrm{TE/T2_{ic}}} \\ \mathrm{S_{ec}} = \mathrm{e}^{-[\mathrm{bD_{ec;\perp}}(\mathbf{n}\cdot\mathbf{u}) + \mathrm{bD_{ec;\parallel}}\,(1-(\mathbf{u}\cdot\mathbf{n})^2)]} \cdot \mathrm{e}^{-\mathrm{TE/T2_{ec}}} \end{cases} \tag{5.6}$$

Secondly, the intra-axonal radial diffusivity is given by:

$$\mathrm{D_{ic;\perp}}(\mathrm{q}(\omega), \mathrm{D}(\omega)) = \mathrm{D_{ic;\perp}}(\mathrm{q}(\omega)|\mathrm{D}_\infty, \sigma, \mathrm{p}) = \frac{\int |\mathrm{q}(\omega)|^2 \mathrm{D}(\omega)\,\mathrm{d}\omega}{\mathrm{b}} \tag{5.7}$$

The expression on the right side corresponds to the diffusion coefficient computed from the signal within the spectral analysis (Sec. 4.3).

The model inherits 11 free model parameters from the Open model, adds 3 extra parameters corresponding the axonal trajectories and intra- and extra-cellular $\mathrm{T}_2$ decay constants, in total 16 free parameters.

# Chapter 6

# Methods & Approaches

In this section a 1D-toy model of axonal trajectories is introduced, and its influence is studied on the diffusion spectra by numerical simulations. Non-straight axonal trajectories are used to investigate limitations of a model that assumes straight-axonal trajectories. The model of axonal trajectories incorporated into a model of brain white matter as the *Axonal trajectory model* is then applied to state-of-the-art brain white matter data.

## 6.1 Representation of axonal trajectories

Axonal trajectories were represented as thin non-permeable 1D undulating wires with a position given by:

$$\mathrm{y(x)} = \mathrm{A} \cdot \sin(\Phi) = \mathrm{A} \cdot \sin\left(2\pi \cdot \frac{\mathrm{x}}{\lambda} + \mathrm{r(x)}\right) \tag{6.1}$$

with amplitude in the range of a = [1;10] µm, wavelengths in the range of $\lambda$ = [5;200] µm and a stochastic part, r(x), generated by cumulative sum of random numbers with different degree of correlation. Intra-axonal diffusivity $\mathrm{D_i} = 1.7\,\mu\mathrm{m}^2/\mathrm{ms}$ was assumed.

Two types of axonal trajectories can be differentiated:

- Harmonic axonal trajectories characterized by amplitude A and wavelength $\lambda$, i.e. r(x) = 0.
- Stochastic axonal trajectories characterized by non-zero stochastic part, i.e. r(x) $\neq$ 0.

Characteristics of the model were studied only in the perpendicular direction to the propagation of axons.

## 6.2 Numerical simulations

Reality can be modeled in-silico and simulations have high informational value [51]. If the physics of the system is well understood, the numerical simulations may provide a way to study relations between variables under well-controlled conditions.

### 6.2.1 Monte Carlo simulations

Monte Carlo simulations track characteristics of motion of random walkers in a specified environment. In each time interval, the walkers move in a random direction. Primary information obtained from the simulations are thus the spatial positions of random walkers at given time and that can be used to calculate other properties. Random walkers can model the diffusion process.

The walkers' individual steps are drawn from a normal distribution with variance $\sigma = 2\mathrm{Ddt_d}$, where $\mathrm{dt_d}$ is the diffusion time step. The Brownian trajectories can be treated, on the length-scale order of picoseconds, as independent random variables and thus, by the central limit theorem, the stepping, at the timescales of the order of milliseconds, averages to a normally distributed random variable. Provided that the walkers can diffuse freely on the order of milliseconds the diffusion is described by a Gaussian distribution with variance $\sigma = 2\mathrm{Dt_d}$.

The movements of the random walkers were simulated one-dimensionally along a straight wire and mapped onto a specific environment whose properties we studied:

$$\mathrm{p} \coloneqq \mathrm{p}_1, \mathrm{p}_2, \ldots \mathrm{p_n}, \ldots, \mathrm{p_N} \text{ and } \mathrm{dp} = \mathrm{p_n} - \mathrm{p_{n-1}} \tag{6.2}$$

$$\mathrm{t} \coloneqq \mathrm{t}_1, \mathrm{t}_2, \ldots, \mathrm{t_j} \ldots, \mathrm{t_J} \text{ and } \mathrm{dt} = \mathrm{t_j} - \mathrm{t_{j-1}} \tag{6.3}$$

The wire was mapped onto a curve $\mathbf{r}$ given by:

$$\mathbf{r}(\mathrm{p}) = (\mathrm{r_x}(\mathrm{p}), \mathrm{r_y}(\mathrm{p})) \coloneqq \mathrm{p2xy}(\mathrm{p}) \tag{6.4}$$

where p2xy is a function that maps a straight wire onto a two-dimensional curve $\mathbf{r}$, parameterized by p.

Two methods of computation of velocity autocorrelation function were implemented:

#### Computation of instantaneous velocities of the random walkers from instantaneous displacements

Velocity autocorrelation function, ac(t), can be computed as the average of initial velocity times every consequent velocity, i.e.

$$\mathrm{v_n}(\mathrm{t_j}) = \frac{\mathrm{x_n}(\mathrm{t_j}) - \mathrm{x_n}(\mathrm{t_{j-1}})}{\mathrm{dt}} \tag{6.5}$$

$$\mathrm{ac}(\mathrm{t_j}) = \langle \mathrm{v_n}(\mathrm{t_j} = 0) \cdot \mathrm{v_n}(\mathrm{t_j}) \rangle = \frac{1}{\mathrm{N}} \sum_{\mathrm{n}}^{\mathrm{N}} \mathrm{v_n}(\mathrm{t_j} = 0) \cdot \mathrm{v_n}(\mathrm{t_j}) \tag{6.6}$$

#### Computation of mean square displacement msd(t) of the random walkers from their instantaneous positions

The velocity autocorrelation function can be computed as:

$$\mathrm{msd}(\mathrm{t_j}) = \frac{1}{\mathrm{N}} \sum_{\mathrm{n}}^{\mathrm{N}} (\mathrm{x_n}(\mathrm{t_j} = 0) - \mathrm{x_n}(\mathrm{t_j}))^2 \tag{6.7}$$

$$\mathrm{ac}(\mathrm{t}) = \langle \mathrm{v}(\mathrm{t} = 0) \cdot \mathrm{v}(\mathrm{t_j}) \rangle = \frac{1}{2} \frac{\mathrm{d}^2}{\mathrm{dt}^2} \mathrm{msd}(\mathrm{t}) \tag{6.8}$$

In our simulations, lag $\tau = 1$. The diffusion spectrum was computed as a Fourier transform of the autocorrelation function (Eq. 4.3).

### 6.2.2 Gaussian sampling

Whenever possible, analytical approaches should be preferred. Another way to compute mean square displacement, perhaps closer to analytical approach, is a method that we termed Gaussian sampling. Gaussian sampling relies on simulating and averaging over different diffusion particle trajectories weighted by a Gaussian function. More specifically, for each position $\mathrm{x_n}$ and each time-point $\mathrm{t_j}$ a diffusion trajectory is computed, and the displacements are weighted by a Gaussian distribution with variance $\sigma = \sqrt{2\mathrm{D_0 t_j}}$. It is an analytical computational method in the sense that it does not rely on drawing stochastic numbers from a distribution.

Gaussian sampling can be described by a pseudo-algorithm:

*For each spatial position on the curve r*
*For each diffusion time* $\mathrm{t_d}$
- *Compute diffusion trajectory within sampling width on the curve* $\mathbf{r}$*;*
- *Weight all the trajectories within the sampling width by a Gaussian function with variance* $2\mathrm{Dt_d}$*;*
- *Compute mean square displacements (msd);*
- *Sum all msd contributions;*

*End*
*End*
- *Average over all spatial points;*

## 6.3 Diffusion spectra of axonal trajectories

### 6.3.1 Numerical simulations of diffusion spectra of axonal trajectories

Simulations in synthetically generated structures, that intended to mimic the harmonic axonal trajectories, were performed for amplitudes $\mathrm{a} = 1, 2, 3, 4\,\mu\mathrm{m}$ and wavelengths $\lambda = 25, 50, 75, 100, 125, 150\,\mu\mathrm{m}$ by Monte Carlo simulations by computing the mean square displacement.

Simulations in synthetically generated structures, that are intended to mimic the stochastic axonal trajectories, were performed at first by trial and error. However, when the dependence of diffusion spectra parameters on the axonal trajectory parameters was

found, a microscopical orientation dispersion μOD = 0.01, 0.03 (Eq. 4.15) and dispersion-weighted wavelength = 20 µm, 40 µm (Eq. 4.20) was chosen.

Algorithms must terminate in a finite time. However, the numerical approaches of diffusion spectra computation require knowledge of particle positions at any time, including infinitely long times. Long time intervals of the mean square displacement correspond to the low frequencies in the diffusion spectrum, namely the zero frequency to infinitely long time. That cannot be achieved by the numerical methods described above.

For restricted diffusion, there exist a workaround. Since $D(t \to \infty) = 0$, $D(\omega) = 0$ as $\omega \to 0$.

To ensure the ergodicity of the velocity autocorrelation function is satisfied, the walkers were initiated in the case of harmonic axonal trajectories in at least one period of the sine wave. The ergodicity in the case of stochastic axonal trajectories was ensured by initiating the walkers in at least 200 realizations of the possible distribution of stochastic axonal trajectories.

### 6.3.2 Diffusion spectra approximation

Numerically obtained diffusion spectra were fitted a phenomenological fit function of the form:

$$D(\omega|D_\infty, \sigma, p) = D_\infty \left(1 - e^{-\frac{\omega^p}{\sigma^2}}\right) \tag{6.9}$$

Where $D_\infty$, $\sigma$ and p are the three fit parameters. $D_\infty$ is called spectral height, spectral width $\omega$ can be computed from $\sigma$ as $\omega = (-\sigma^2 \log 1/2)^{1/p}$ and p corresponds to power behavior in the low frequency part (Fig. 6.1).

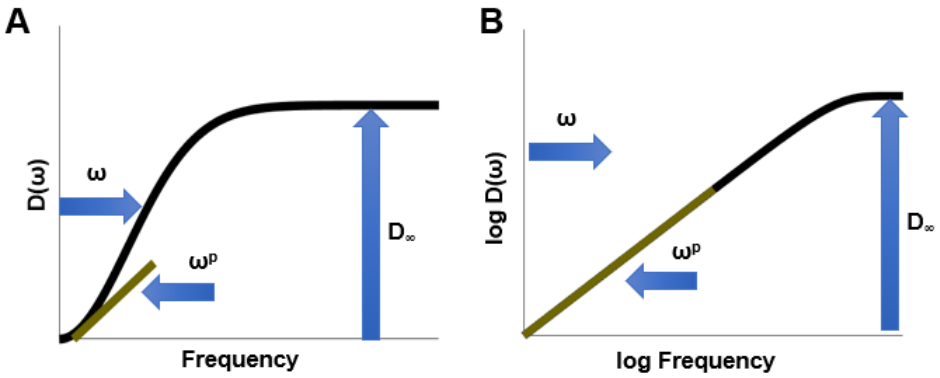


Figure 6.1: **Parameters of diffusion spectra. A:** Width of the spectra $\omega$ at half-width-half maximum; height of the spectra at high frequencies $D_\infty$ that represents diffusivity at short diffusion times, and power law behavior at low frequencies: power p in $\omega^p$. **B:** Same diffusion spectrum in a loglog plot.

The form of fit equation introduces another constraint. The limiting behavior of $D(\omega)$ when $\omega \to 0$ is $D(\omega) \to 0$. That means the fit equation is not suited in the cases where such behavior is not expected. The limiting behavior of $D(\omega)$ when $\omega \to \infty$ is $D(\omega) \to$

const. The limiting behavior of diffusion spectra of the axonal trajectories has the same properties as the limiting behavior of the fit equation which is another argument why the fit equation is suited for this type of geometry.

The appropriateness of the fit was assured on two different levels. Firstly, the numerical simulations were conducted for a larger range of parameters for many possible axonal trajectories and the same functional form of diffusion spectra was observed. Secondly, the simulated signal was obtained from the fitted diffusion spectra was compared to a more robust (but less predictive) way of signal computation, to Monte Carlo phase accrual simulations (i.e. implemented Eq. 3.21 and Eq. 3.22).

### 6.3.3 Characterization of diffusion spectra of axonal trajectories

This part was submitted as an abstract to the joint conference of International Society for Magnetic Resonance in Medicine and ESMRMB (*ISMRM - ESMRMB 2018*).

Based on the analysis of the diffusion within sine waves (Sec. 4.4.3), a model for the harmonic axonal trajectories, we hypothesized that the results apply also to stochastic axonal trajectories.

The descriptive parameters were predicted from the trajectories themselves. The spectral width was predicted as:

$$\omega_{\text{predicted}} = \lambda_{\sigma}^{-2} \cdot \mathrm{D}_0 = \left( \frac{\langle \mu\mathrm{OD}(\mathrm{x}_0) \cdot \lambda^{-1}(\mathrm{x}_0) \rangle}{\mu\mathrm{OD}} \right)^{-2} \cdot \mathrm{D}_0 \tag{6.10}$$

Spectral height was predicted as:

$$\mathrm{D}_{\infty;\text{predicted}} = \langle \mu\mathrm{OD}(\mathrm{x}) \rangle \cdot \mathrm{D}_0 \tag{6.11}$$

Power law behavior $\omega^{\mathrm{p}}$ was not predicted, but obtained as a fit parameter p (Eq. 6.9).

The effect varying correlation length of axonal trajectories, defined as the decay rate of the envelope of square of autocorrelation function of y(x), on their corresponding diffusion spectra was also studied.

## 6.4 Fitting the Axonal trajectory model

The analyzed data of corpus callosum were acquired for a competition White matter modeling challenge that was held during the International Symposium on Biomedical Imaging (*ISBI*) in 2015 [53].

The $\mathrm{T}_{2;\mathrm{ic}}$ and $\mathrm{T}_{2;\mathrm{ec}}$ were constrained to the same value, $\mathrm{T}_{2;\mathrm{ic}} = \mathrm{T}_{2;\mathrm{ec}}$ and other parameters to maximal but biologically plausible values.

Outlier strategy was employed. The model was fitted, the sum of square differences between the measured signal, the predicted signal (SSE) was computed and data points with SSE $> 500$ were discarded and the model was refitted.

The range of parameters of axonal trajectories, to which the signal can be sensitized, was inspected by plotting the power spectra of the gradient waveforms. To probe the whole parameter space, the model was constrained to a unique combination of $D_\infty$, $\omega$, p and the rest of the free parameters were fitted. The sum of square differences between the measured signal and the predicted signal (SSE) was computed and plotted for each combination of constrained parameters.

## 6.5 Influence of non-straight axonal trajectories on models that assume straight cylinders

This part was addressed as an abstract and oral presentation at *ESMRMB 2017* conference.

Simulations of harmonic axonal trajectories were performed to obtain signal and diffusion spectra (Fig. 6.2). Parameters for the simulated dMRI experiments are summarized in Tab. 6.1. Amplitudes a = 1 – 4 µm and the wavelength $\lambda = 50$ µm were chosen to mimic the undulations in corpus callosum. Axonal diameters were estimated by fitting the simulated signal intensities by ActiveAx model, constrained to the case of intra-axonal diffusion only.

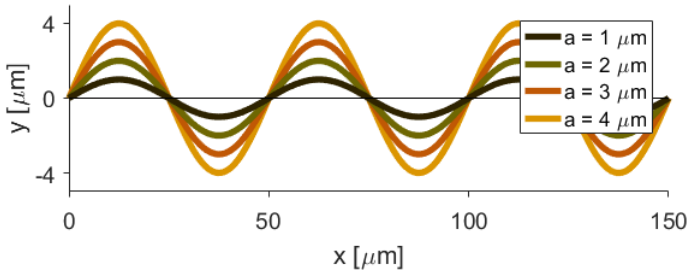


Figure 6.2: **Simulation geometries.** Axons are represented by harmonic axonal trajectories with wavelength $\lambda = 50$ µm and amplitudes A = [1; 4] µm. Signal and diffusion spectra were calculated in the perpendicular y-direction.

Table 6.1: **Parameters for the simulated dMRI experiments [16].**

| **Waveform** | **0$^{th}$** | **1$^{st}$** | **2$^{nd}$** | **3$^{rd}$** | **4$^{th}$** |
|---|---|---|---|---|---|
| **\|G\| [mT/m]** | 0 | 58 | 46 | 57 | 60 |
| **$\delta$ [ms]** | 0 | 12 | 15 | 5 | 13 |
| **$\Delta$ [ms]** | 0 | 80 | 77 | 87 | 20 |
| **b [s/mm$^2$]** | 0 | 2634 | 2453 | 496 | 682 |

Furthermore, the Axonal trajectory model was modified to mimic the constraints imposed in the ActiveAx and applied to the same data. The same outlier strategy as in the case of fitting the Axonal trajectory model was employed. The model was constrained to have the same $T_2$ value in all 4 compartments.

# Chapter 7

# Results

The numerical methods are validated and the effects of axonal trajectories on diffusion spectra are studied. Estimated and predicted parameters of diffusion spectra are compared and the effects of non-straight axonal trajectories on a model assuming straight axonal trajectories explained through their diffusion spectra. Lastly, the Axonal trajectory model is validated and fitted to the experimental data.

## 7.1 Simulation of the diffusion spectra in different trajectories

The diffusion spectra can be computed numerically, and the Gaussian Sampling method (Sec. 6.2.2) is the most suitable one. The diffusion spectra can be characterized by the fit equation Eq. 6.9 that captures the functional form. The coefficients of the fit equation Eq. 6.9 can be linked to parameters describing the parameters of axonal trajectories.

### 7.1.1 Comparison and validation of numerical methods

Diffusion spectra computed by different numerical methods are aligned with the analytical prediction (Fig. 7.1A). The methods are also qualitatively compared among each other to inspect how they introduce noise into the results (Fig. 7.1B).

Gaussian Sampling introduces the least noise into the numerically obtained diffusion spectra, followed by Monte Carlo (computation of mean square displacement) and Monte Carlo (computation of instantaneous velocities). The last method was discarded.

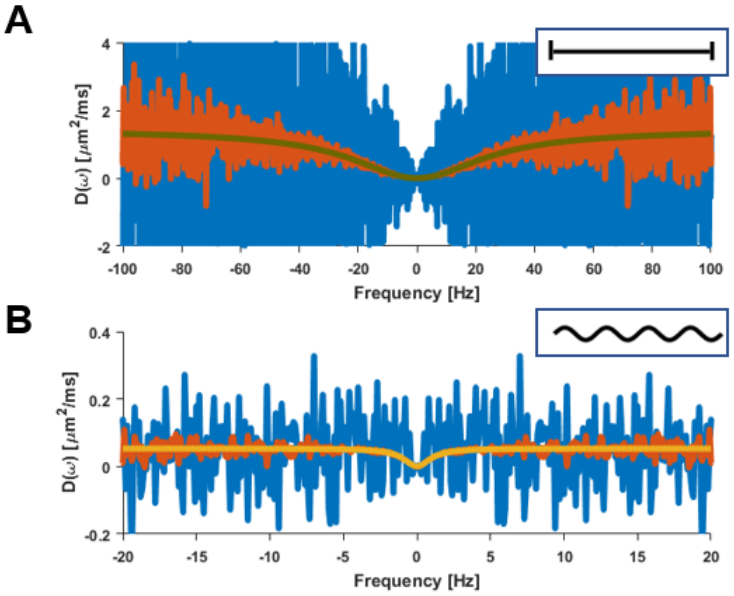


Figure 7.1: **Comparison of numerical methods. A: Comparison of numerical methods with the analytical prediction.** Diffusion spectra of 1D planar restricted geometry were computed by Monte Carlo simulations from instantaneous velocities (blue) and mean square displacement (red). Monte Carlo simulations are aligned with the analytical prediction (green), however, the computation of instantaneous velocities introduced substantial noise into the results and is thus not well suited for this type of simulations. The simulations were computed for the same discretization parameters with the same computational time. **B: Comparison of numerical methods on axonal trajectories.** Diffusion spectra of a harmonic axonal trajectory (characterized by $\lambda = 100\,\mu m$, $a = 4\,\mu m$) were computed by Monte Carlo simulations from instantaneous velocities (blue), mean square displacements (red) and by Gaussian Sampling (yellow). The diffusion spectra are aligned; however, the computation of instantaneous velocities introduces substantial noise into the results and is thus not well suited for this type of simulations. They were computed for similar discretization parameters with similar computational time.

### 7.1.2 Diffusion spectra of axonal trajectories

#### Harmonic axonal trajectories

Diffusion spectra of harmonic axonal trajectories with varying amplitude a (rows) and wavelength $\lambda$ (columns) were generated by Monte Carlo (Fig. 7.2). They were also characterized by the dispersion-weighted wavelength $\lambda_\sigma$ (columns) and microscopic orientation dispersion μOD unique for each axonal trajectory. The simulations introduced noise into the spectra due to the nature of the random walks, notably at higher frequencies.

They bear similar functional dependence but differ in the coefficients associated with their functional form. The slope p and spectral width $\omega$ is similar for the same wavelength $\lambda$ and dispersion-weighted wavelength $\lambda_\sigma$ (column-wise) but spectral height $D_\infty$ is not uniquely associated with a single amplitude (row-wise). It is uniquely associated with microscopic orientation dispersion μOD.

The relevant characteristics of the trajectories are rather the dispersion-weighted wavelength and microscopic orientation dispersion. 3 parameters and the functional dependence are sufficient to describe the diffusion spectra. The predicted spectral width $\omega$ (Eq. 6.10) and spectral height $D_\infty$ (Eq. 6.11) match with the estimated ones.

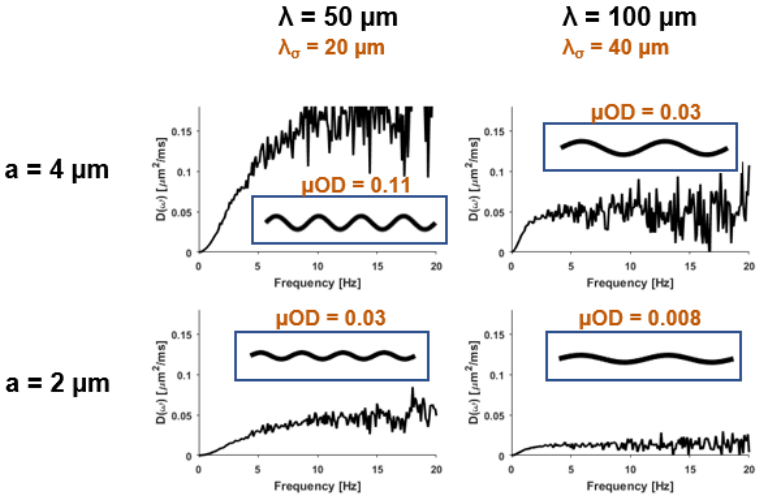


Figure 7.2: **Diffusion spectra of harmonic axonal trajectories.** Harmonic axonal trajectories, parametrized by amplitude a and wavelength $\lambda$, correspond to different diffusion spectra. The origin of the noise can be tracked to the nature of the random walks in the Monte Carlo simulation. The predicted value of spectral width $\omega$ for $\lambda_\sigma = 20\,\mu m$ is $\omega_{est} = 4.3\,Hz$ and for $\lambda_\sigma = 40\,\mu m$ is $\omega_{est} = 1.1\,Hz$. The predicted value of $D_\infty$ for $\mu OD = 0.11$ is 0.18 $\mu m^2/ms$ and for $\mu OD = 0.03$ is 0.05 $\mu m^2/ms$, for $\mu OD = 0.008$ is 0.014 $\mu m^2/ms$. Predicted values correspond to the estimated ones. The slight discrepancy between predicted and estimated values in the $\lambda = 50\,\mu m$, $a = 4\,\mu m$ (top row, left column) may be caused by inadequate spatial and temporal discretization.

### Stochastic axonal trajectories

Diffusion spectra of stochastic axonal trajectories with varying microscopic orientation dispersion µOD (rows) and dispersion-weighted wavelength $\lambda_\sigma$ (columns) were generated by Gaussian Sampling (Fig. 7.3). Each axonal trajectory was also characterized by its maximal amplitude $a_{max}$ but their wavelengths $\lambda$ could not have been defined. Unlike Monte Carlo, Gaussian sampling introduced little noise into the spectra.

They bear similar functional dependence but differ in the coefficients associated with their functional form. The slope p and spectral width $\omega$ in each column is similar for the same dispersion-weighted wavelength $\lambda_\sigma$ (column-wise) and spectral height $D_\infty$ is similar for the same microscopic orientation dispersion µOD (row-wise).

The relevant characteristics of the trajectories are the dispersion-weighted wavelength and microscopic orientation dispersion. 3 parameters and the functional dependence are sufficient to describe the diffusion spectra of the stochastic axonal trajectories. The predicted spectral width $\omega$ and spectral height $D_\infty$ match their estimates. The spectral width $\omega$ of stochastic axonal trajectories matches harmonic axonal trajectories for the same dispersion weighted-wavelength $\lambda_\sigma = 20\,\mu m$.

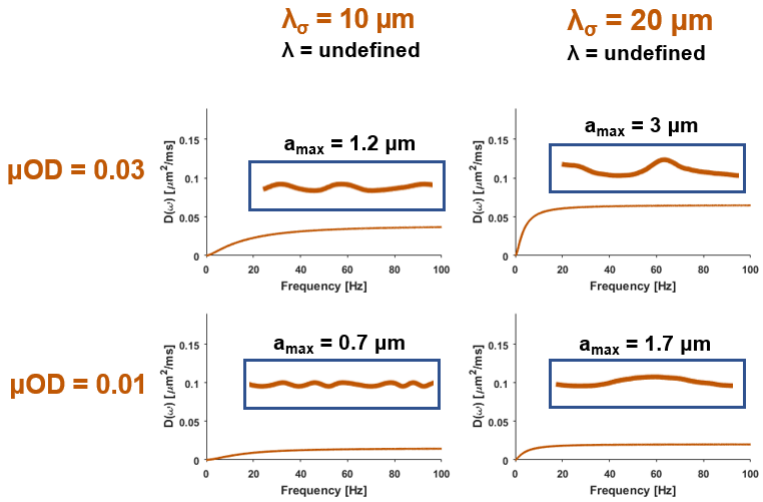


Figure 7.3: **Diffusion spectra of stochastic axonal trajectories.** Stochastic axonal trajectories, parametrized by varying microorientation dispersion µOD and dispersion-weighted wavelength $\lambda_\sigma$, correspond to different diffusion spectra. Unlike in the previous case the spectra are almost noise-free because instead of Monte Carlo simulations the Gaussian Sampling method was used to generate the spectra. The predicted value of spectral width $\omega$ for $\lambda_\sigma = 10\,\mu m$ is $\omega_{est} = 17\,Hz$ and for $\lambda_\sigma = 20\,\mu m$ is $\omega_{est} = 4.3\,Hz$. The predicted value of $D_\infty$ for µOD = 0.03 is $0.05\,\mu m^2/ms$ and for µOD = 0.01 is $0.017\,\mu m^2/ms$. Estimated and predicted values correspond well. The slight discrepancy between predicted and estimated values in the $\lambda_\sigma = 10\,\mu m$, µOD = 0.03 (top row, left column) may be caused by inadequate sampling.

### 7.1.3 Diffusion spectra approximation

The relevant properties of the diffusion spectra can be captured by a 3-parameter fit equation (Eq. 6.9) both in the harmonic axonal trajectories, as well as in the stochastic axonal trajectories. The parameters of the approximation, together with associated spectral width $\omega$, are listed in Tab. 7.1 and Tab. 7.2.

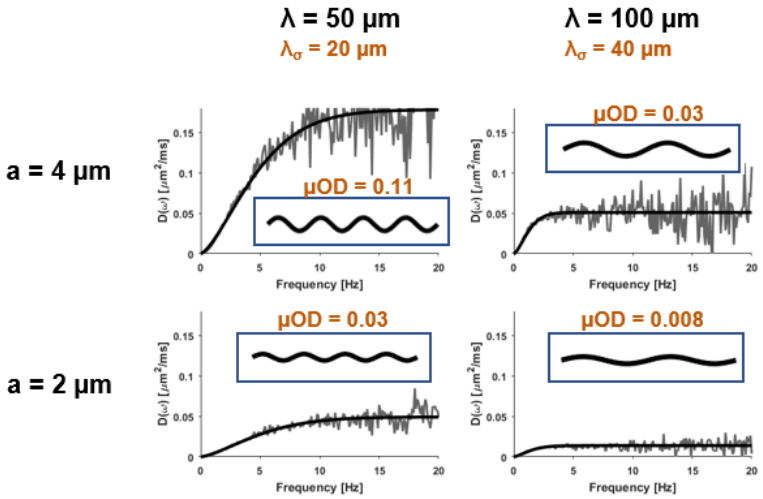


Figure 7.4: **Diffusion spectra approximation of harmonic axonal trajectories.** The numerically obtained diffusion spectra (Fig. 7.2) were approximated by Eq. 6.9.

Table 7.1: **Parameters of approximated diffusion spectra of harmonic trajectories.** $[D_\infty] = [\mu m^2/ms]$.

| | $\lambda = 50\,\mu m$ | | $\lambda = 100\,\mu m$ | |
|---|---|---|---|---|
| $a = 4\,\mu m$ | $\sigma = 3.4$<br>$D_\infty = 0.17$<br>$p = 1.45$ | $\omega = 4.4\,Hz$<br>$\mu OD = 0.11$ | $\sigma = 1.4$<br>$D_\infty = 0.05$<br>$p = 1.45$ | $\omega = 1.1\,Hz$<br>$\mu OD = 0.03$ |
| $a = 8\,\mu m$ | $\sigma = 3.6$<br>$D_\infty = 0.05$<br>$p = 1.47$ | $\omega = 4.2\,Hz$<br>$\mu OD = 0.03$ | $\sigma = 1.3$<br>$D_\infty = 0.01$<br>$p = 1.51$ | $\omega = 1.3Hz$<br>$\mu OD = 0.008$ |

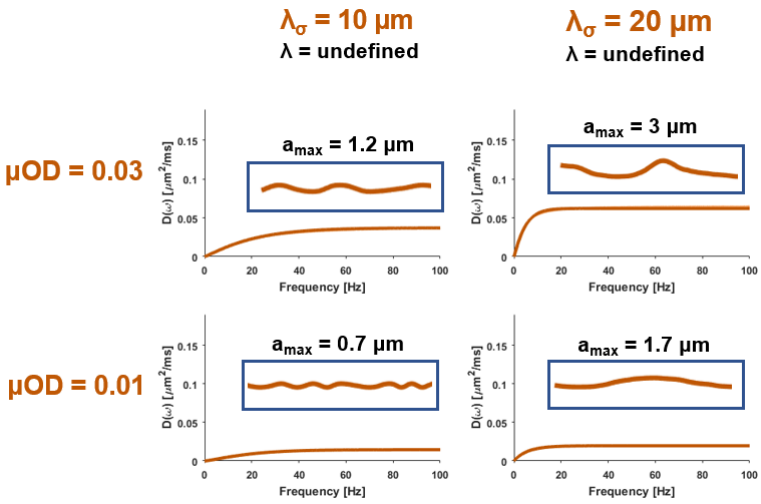


Figure 7.5: **Diffusion spectra approximation of stochastic axonal trajectories.** The numerically obtained were approximated by the Eq. 6.9. Gaussian sampling, compared with Monte Carlo, adds relatively little noise into the results. The numerically computed diffusion spectra (Fig. 7.3) are overlaid by the fit equation.

Table 7.2: **Parameters of approximated diffusion spectra of stochastic trajectories.** $[D_\infty] = [\mu m^2/ms]$.

| | $\lambda_\sigma = 10\,\mu m$ | | $\lambda_\sigma = 20\,\mu m$ | |
|---|---|---|---|---|
| **µOD = 0.03** | $\sigma = 5.5$<br>$D_\infty = 0.037$<br>$p = 1.13$ | $\omega = 14.8\,Hz$<br>$a_{max} = 1.2\,\mu m$ | $\sigma = 2.36$<br>$D_\infty = 0.064$<br>$p = 1.05$ | $\omega = 3.6\,Hz$<br>$a_{max} = 3\,\mu m$ |
| **µOD = 0.01** | $\sigma = 6.46$<br>$D_\infty = 0.015$<br>$p = 1.25$ | $\omega = 14.8\,Hz$<br>$a_{max} = 0.7\,\mu m$ | $\sigma = 2.4$<br>$D_\infty = 0.017$<br>$p = 1$ | $\omega = 4\,Hz$<br>$a_{max} = 1.7\,\mu m$ |

## 7.2 Quantification of the diffusion spectra properties

This part was submitted as an abstract to the joint conference of International Society for Magnetic Resonance in Medicine and ESMRMB (*ISMRM - ESMRMB 2018*).

To answer which physical properties can be fundamentally contained in the diffusion spectra, the predicted and estimated diffusion spectra characteristics were compared for wide range of axonal trajectories.

### 7.2.1 Predicted and estimated diffusion spectra parameters

Characteristics of the trajectories had a clear effect on the diffusion spectra (Fig. 7.6). The estimated width and height of the diffusion spectra agreed well with the values predicted

from the trajectories (Fig. 7.6A). The width was determined by the average wavelength of the undulating trajectories, weighted by the local orientation dispersion (Fig. 7.6B). The power law exponent was found to vary between 1 and 2 for different trajectories (Fig. 7.6C).

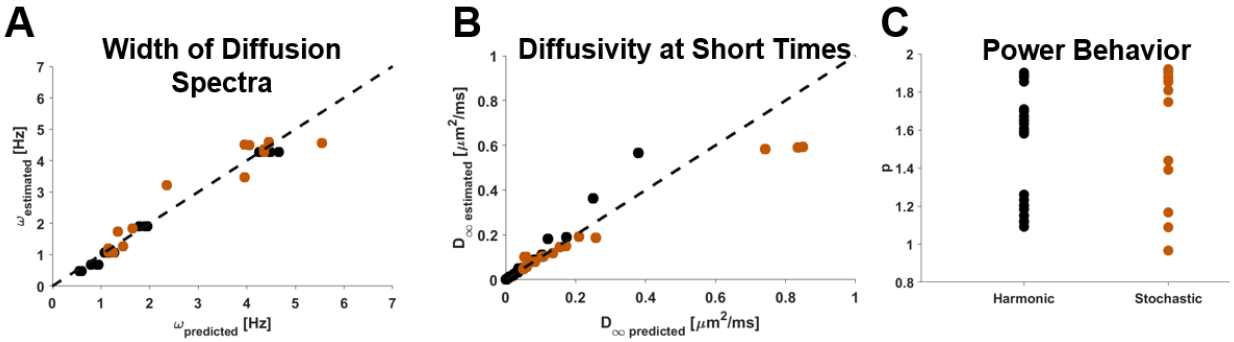


Figure 7.6: **Predicted and estimated parameters of the diffusion spectra. A:** spectral width ($\omega$), **B:** spectral height ($D_\infty$) and **C:** power behavior (p). Black points correspond to harmonic trajectories, beige to stochastic. Overall, the predicted and estimated parameters match. Power behavior at low frequency is a distribution, not a single power.

### 7.2.2 Effects of correlation length

Correlation length, unless microscopic orientation dispersion or dispersion-weighted wavelength changes, does not have any significant effect on the resulting diffusion spectra (Fig. 7.7). That is congruent with the expression predicting the diffusion spectra parameters since they do not explicitly contain the correlation length.

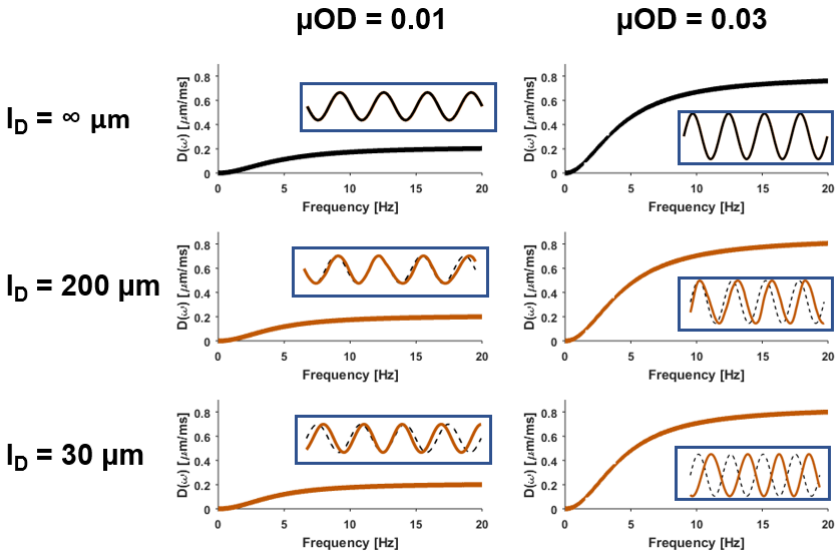


Figure 7.7: **Correlation Length.** Diffusion spectra of stochastic axonal trajectories were generated and characterized by their correlation lengths (rows) and variable microscopic orientation dispersions (columns). Shorter correlation lengths indicate a more disordered trajectory, but contrary to our intuition, it did not lead to significant changes in the width of the diffusion spectra. However, disorder could change the microscopic orientation dispersion and dispersion-weighted wavelength which would, indeed, lead to higher diffusivities at short diffusion times $D_\infty$ and to changed spectral width $\omega$. The spectra from the different trajectories within each column are indistinguishable, meaning that diffusion experiments cannot be used to tell them apart.

## 7.3 The impact of neglecting and including trajectorial characteristics

When non-straight axonal trajectories are provided to a model, that estimates axonal diameter but assumes straight axonal trajectories, the estimated diameter is significantly overestimated despite that the goodness of fit is relatively high. That may be explained by the similarity of the diffusion spectra in the low frequency part of spectra associated with cylinders and axonal trajectories.

### 7.3.1 Neglecting axonal trajectories

#### Influence of non-straight axonal trajectories on models that assume straight cylinders

This part was addressed as an abstract and oral presentation at the European Society for Magnetic Resonance in Medicine and Biology (*ESMRMB 2017*) conference.

Generated signal-versus-b curves of the harmonic axonal trajectories were fitted to the ActiveAx model. Diameters estimated by ActiveAx were strongly correlated with the

undulation amplitudes (Fig. 7.8). The ActiveAx interpreted the undulation amplitudes as cylinder diameters. The axonal trajectories provided to the model have associated diameter $d = 0$, nonetheless, $d \gg 0$ was estimated.

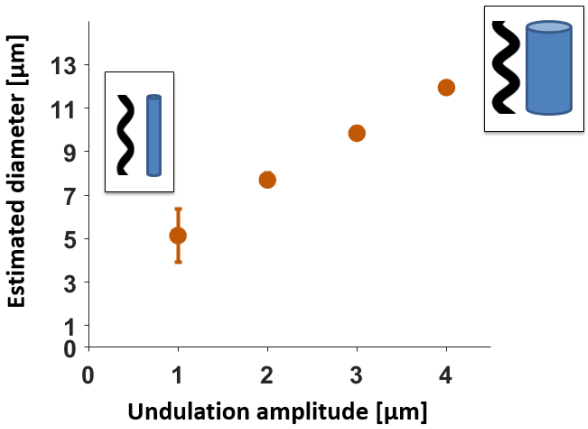


Figure 7.8: **Estimated diameters.** Larger undulation amplitudes are interpreted by the ActiveAx model as cylinders with larger diameters and vice versa. The diameter of the axonal trajectories is $d = 0$, the ActiveAx estimates $d \gg 0$. Error bars indicate one standard deviation.

The effect can be analyzed from the time-dependent perspective. The diffusion spectra corresponding to undulation patterns are similar to the spectra corresponding to cylinders at low frequencies but differ at high frequencies (Fig. 7.9).

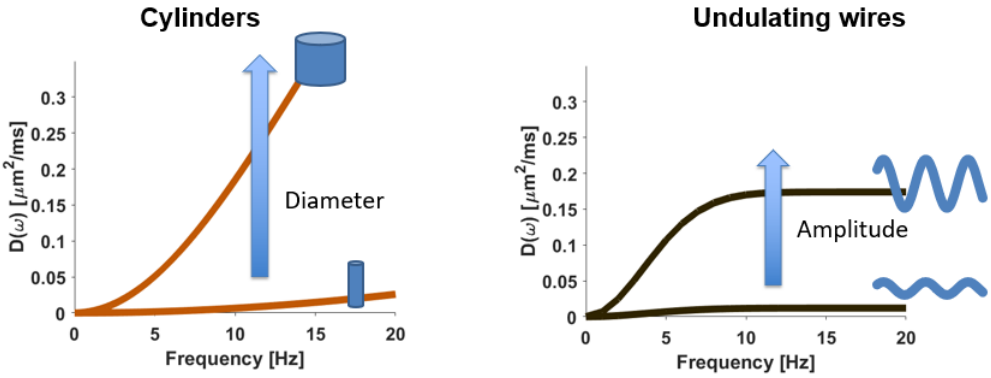


Figure 7.9: **Diffusion spectra of cylinders and harmonic axonal trajectories.** Diffusion spectra associated with cylinders and harmonic axonal trajectories are similar at low frequencies. Harmonic axonal trajectories were generated with the same wavelength $\lambda = 50\,\mu m$.

The model seeks for a diffusion spectrum curve associated with a cylinder that matches as closely as possible the diffusion spectrum of the trajectory in the sensitivity region dictated by the encoding spectrum. At higher frequencies the curves are different and thus the diffusion spectrum of a cylinder does not match the diffusion spectrum of the axonal trajectory (Fig. 7.10).

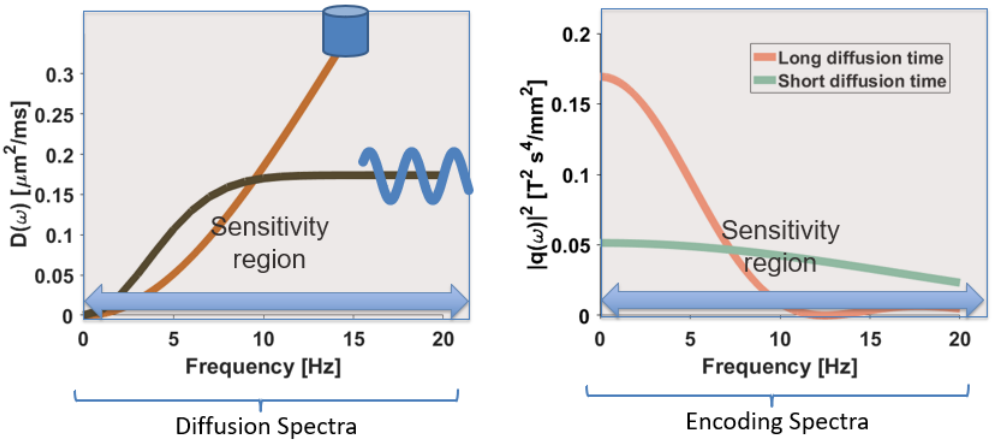


Figure 7.10: **Fitting the ActiveAx, short-diffusion times.** When both long- and short-diffusion time gradients are applied, the encoding spectra sensitize the signal to a frequency range [0; 20 Hz]. Within this range, there is no such diffusion spectrum associated with a cylinder that would closely correspond to the diffusion spectrum of the harmonic axonal trajectory.

At low frequencies the spectra are similar and thus it is possible to find closely matching curves, i.e. the goodness of fit is better than in the previous case (Fig. 7.11). That does not mean, however, the estimated diameter is correct.

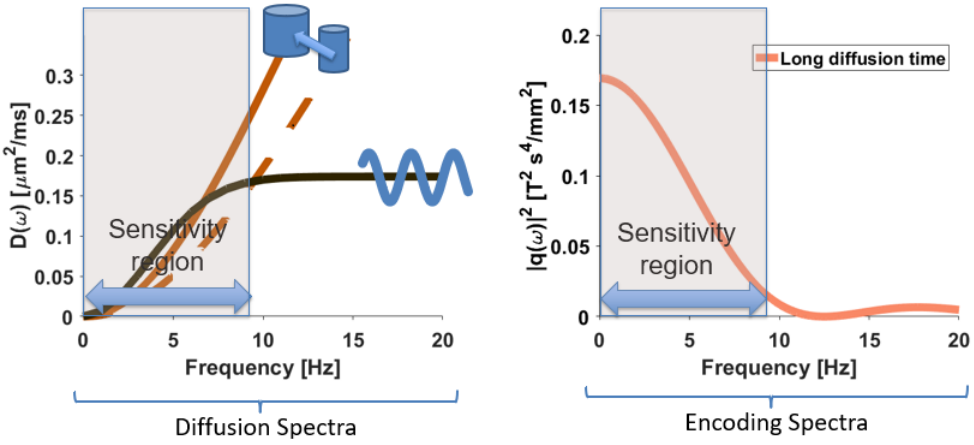


Figure 7.11: **Fitting the ActiveAx, long-diffusion times.** When only long-diffusion time gradient is applied, the estimated diameter is higher and goodness of fit better. The reason is that the encoding spectra sensitize the signal to a narrower frequency range [0; 10 Hz] where the two curves match closely. Better goodness of fit is not, however, indicative of the correctness of the model.

Furthermore, the Axonal trajectory model was modified to include the same constraints as ActiveAx and applied to the same data. The estimated axonal diameter was 7.3 µm with sum of square differences between the measured signal and the predicted signal SSE = 55. The estimated value is far outside of predicted one (Tab. 4.1).

### 7.3.2 Including axonal trajectories

#### Verification of Axonal trajectory model

Signal-vs-b curves of harmonic axonal trajectories were generated by two distinct methods. Firstly, from the Axonal trajectory model, constrained to radial intra-axonal part only and, secondly, by the phase accrual (Monte Carlo; implemented Eq. 3.21 and Eq. 3.22). The Signal-vs-b curves matched which indicates that the coding is correct.

The gradients do not provide a specific contrast in the region below 10 Hz (Fig. 7.12A). The harmonic axonal trajectories characterized by $\lambda = 100\,\mu m$ are associated a small spectral width ($\omega \approx 1\,Hz$) which leads to the relative under-representation of the spectral width $\omega$ parameter in the signal (Fig. 7.12B; right column).

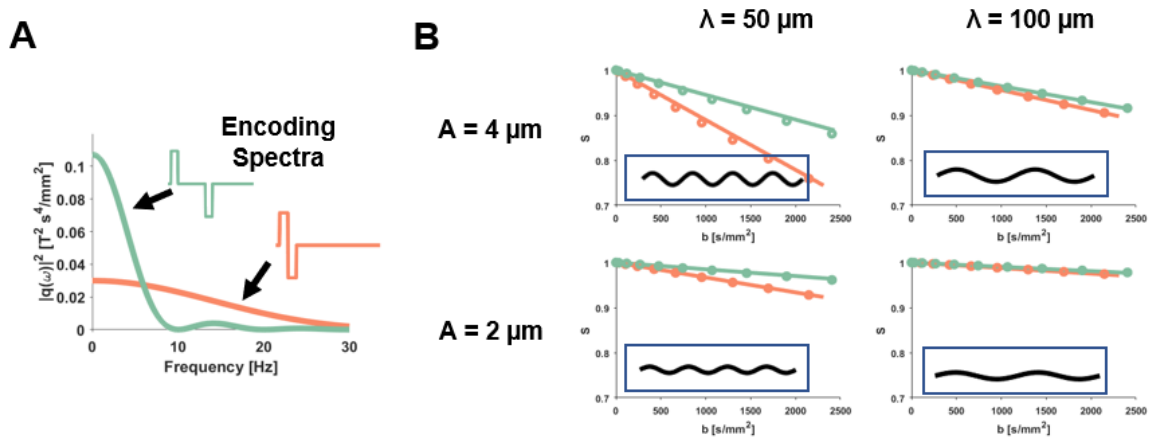


Figure 7.12: **Model validation. A:** Signal-vs-b curves of harmonic axonal trajectories were generated for encoding gradient that probes short diffusion times (red) and long diffusion times (green) with approximately the same b-value. **B:** Solid lines correspond to the signal produced by the Axonal trajectory model and dots by the Monte Carlo phase accrual method. The signal curves are aligned. Moreover, as none of the gradients provide a specific contrast in the frequency below 10 Hz the effects of small $\omega$ become increasingly negligible. The signal becomes dominated only by $D_\infty$ (right column). The figure thus also illustrates the transition from a restriction (left column; both $\omega$, $D_\infty$ parameter encoded into the signal) to orientation dispersion (right column; only $D_\infty$ encoded). Corresponding diffusion spectra are shown in Fig. 7.4.

#### Estimating diffusion spectra parameters

The encoding spectra corresponding to the gradient waveforms were plotted to inspect the maximal parameters of axonal trajectories that could be theoretically be estimated from the signal.

The gradients used to acquire the data sensitize the signal only up to frequency 50 Hz (Fig. 7.13). The diffusion spectra can thus attain any values at frequencies higher than 50 Hz without influencing the signal. It is only feasible to estimate parameters of the diffusion spectra that have spectral width $\omega$ approximately up to 35 Hz which corresponds to axonal trajectories characterized by $\lambda_\sigma < 7\,\mu m$, or in the case of harmonic

axonal trajectories to $\lambda < 17.5\,\mu m$. Axonal trajectories with lower dispersion-weighted wavelength, $\lambda_\sigma < 7\,\mu m$, cannot be reliably estimated from the data.

No gradients provide a specific contrast in the frequency range below 8 Hz (Fig. 7.13). Diffusion spectra characterized by the spectral width $\omega$ below approximately 5 Hz cannot be thus estimated from the data either. Spectral width $\omega < 5\,Hz$ corresponds to axonal trajectories characterized by $\lambda_\sigma > 18\,\mu m$, or in the case of axonal trajectories to $\lambda > 45\,\mu m$. Axonal trajectories with higher dispersion-weighted wavelength, $\lambda_\sigma > 18\,\mu m$, cannot be estimated from the data.

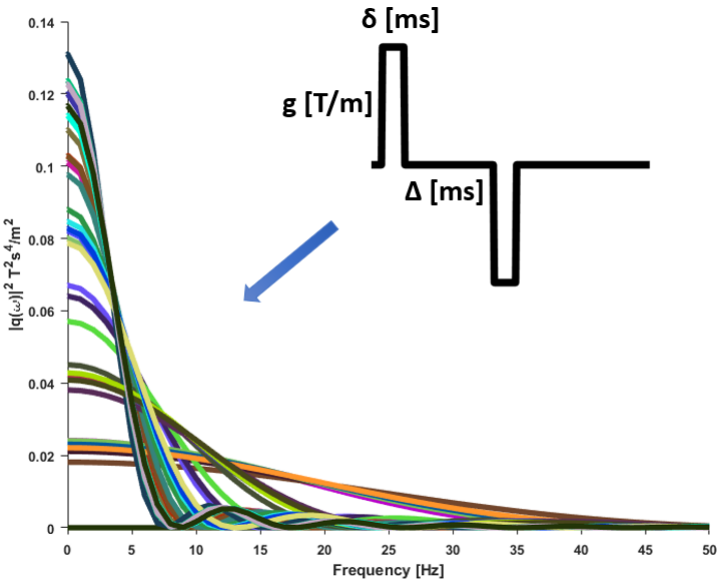


Figure 7.13: **Encoding spectra.** In total 3311 Stejskal-Tanner gradient waveforms were used to generate signal. They are defined by parameters g, $\Delta$ and $\delta$ (upper right corner) but can be also characterized by their corresponding encoding spectra (lower left corner). The signal is not sensitized to parts of diffusion spectra beyond 50 Hz and the gradients do not provide a specific contrast in the region below 8 Hz. Encoding spectra were normalized with respect to their area under the curve.

The Axonal trajectory model was constrained a unique set of parameters $D_\infty$, $\omega$, p and the rest of the free parameters was fitted. The differences in the goodness of fit, measured as the sum of square differences between the measured signal and the predicted signal (SSE), are small (Fig. 7.14). It is thus not reliably possible to estimate from the data all three diffusion spectra parameters $D_\infty$, $\omega$, p without invoking constraints on two of them. Moreover, the set of parameters corresponding to the overall lowest SSE is distinctly different from those that correspond to biologically plausible values (Tab. 7.3; #3).

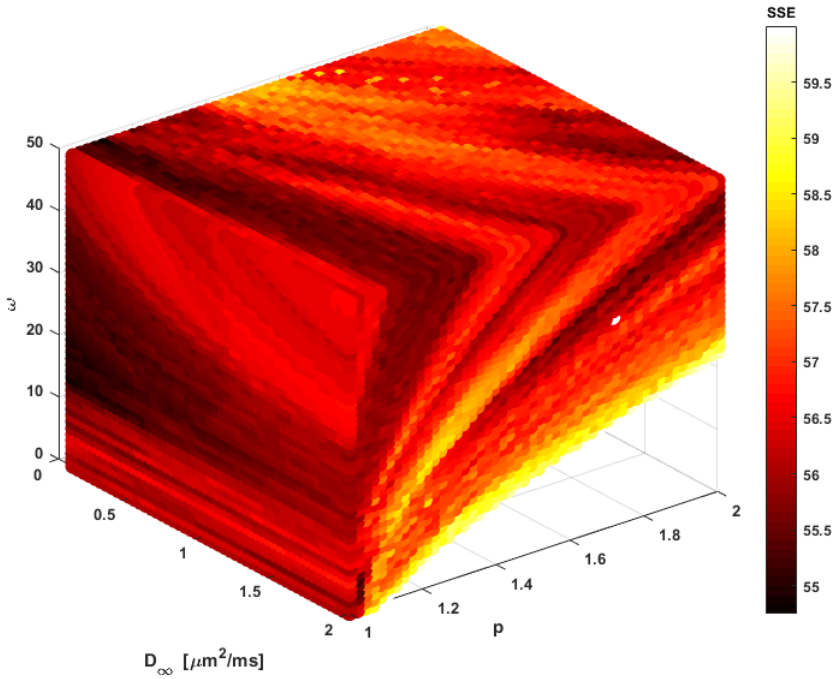


Figure 7.14: **Parameter space.** The Axonal trajectory model was constrained to a set of $D_\infty$, $\omega$, p and the rest of the free parameters was fitted. The sum of square differences between the measured signal and the predicted signal (SSE) is displayed as color scale. Points with SSE $> 60$ were excluded from the plot. The differences in the goodness of fit are small, darker points represent lower SSE values.

### Estimating axonal trajectory parameters

Samples from a posterior distribution of axonal trajectories corresponding to a single set of diffusion spectra parameters were generated. Only statistical descriptors can be estimated from the diffusion spectra parameters, namely microscopic orientation dispersion and dispersion-weighted wavelength, not the exact pathways. Diffusion spectra parameters can correspond to different harmonic trajectories and stochastic trajectories, and, moreover, can correspond to even different stochastic trajectories within the stochastic axonal trajectory category (Fig. 7.15).

If 2 out 3 diffusion spectra parameters are constrained to a biologically plausible value, the estimated third parameter is also biologically plausible (Fig. 7.15).

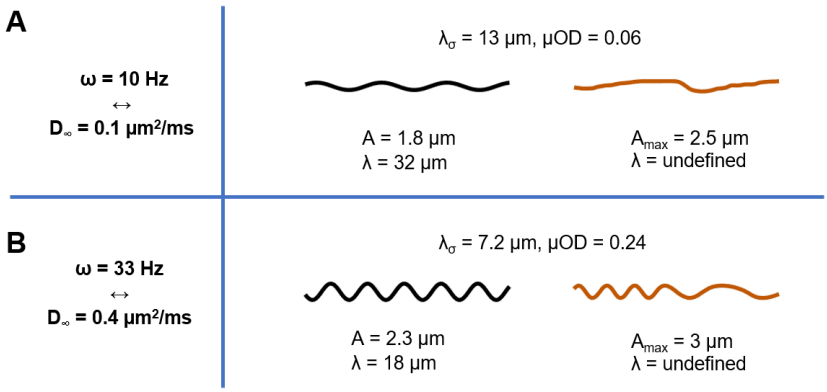


Figure 7.15: **Posterior distribution.** Plausible estimates of an axonal trajectories that could be found in corpus callosum can be obtained from the data (Tab. 4.1). However, a single set of diffusion spectrum parameters corresponds to both a harmonic and a class of stochastic axonal trajectories. **A:** Constraining the model to $\omega = 10\,\mathrm{Hz}$ and $\mathrm{p} = 2$ yield $\mathrm{D}_\infty = 0.1\,\mu\mathrm{m}^2/\mathrm{ms}$ and, vice versa, constraining the model to $\mathrm{p} = 2$ and $\mathrm{D}_\infty = 0.1\,\mu\mathrm{m}^2/\mathrm{ms}$ yield $\omega = 10\,\mathrm{Hz}$. That corresponds to axonal trajectories characterized by $\lambda_\sigma = 13\,\mu\mathrm{m}$ and $\mu\mathrm{OD} = 0.06$. **B:** Same as in A but constraining the model to $\mathrm{p} = 2$ and $\omega = 33\,\mathrm{Hz}$ or $\mathrm{D}_\infty = 0.4\,\mu\mathrm{m}^2/\mathrm{ms}$.

### Estimated values

The model was fitted with 3 distinct set on the constraints of diffusion spectra parameters $\mathrm{D}_\infty$, $\omega$, p. First two (#1, #2) correspond to the setup introduced in the Fig. 7.15 and third (#3) to the values corresponding to the lowest SSE overall (Fig. 7.14). The model contains 13 free parameters. Important free parameters together with their estimated values and corresponding SSE are listed in Tab. 7.3.

Table 7.3: **Free model parameters values.** #1 and #2 correspond to the constrains that yield biologically plausible estimates (described in Fig. 7.15), #3 corresponds to the lowest SSE overall (Fig. 7.14). Note the significant difference between $\mathrm{f_{ic}}$ and $\mathrm{D_{iso}}$ in the case #1, #2 and #3.

| Parameter | Description | #1 | #2 | #3 |
|---|---|---|---|---|
| $\mathbf{f_{ic}}$ | Intra-axonal spin fraction [1] | 0.63 | 0.63 | 0.72 |
| $\mathbf{D_{iso;\,ec}}$ | Extra-axonal isotropic diffusivity [$\mu m^2$/ms] | 1.58 | 1.56 | 1.9 |
| $\mathbf{D_{\Delta;\,ec}}$ | Extra-axonal normalized anisotropy [1] | 0.5 | 0.5 | 0.5 |
| $\mathbf{T_{2;\,ec}}$ | Extra-cellular T2 relaxation time [ms] | 50 | 60 | 60 |
| $\mathbf{T_{2;\,ic}}$ | Intra-axonal T2 relaxation time [ms] | 50 | 50 | 60 |
| $\mathbf{D_{\parallel;\,ic}}$ | Intra-axonal axial diffusivity [$\mu m^2$/ms] | 1.6 | 1.6 | 1.6 |
| $\boldsymbol{\omega}$ | Spectral width [1] | 33.96 | 10 | 5.2 |
| $\mathbf{D_\infty}$ | Spectral height [$\mu m^2$/ms] | 0.4 | 0.1 | 0.13 |
| **p** | Power behavior at low frequencies [1] | 2 | 2 | 1.02 |
| **nf** | Noise fraction [1] | 0.0075 | 0.0076 | 0.0078 |
| **SSE** | Sum of square differences | 56.9 | 56.1 | 54.8 |

# Chapter 8

# Discussion

The estimated parameters of axonal trajectories were congruent with the values predicted by histology (Tab. 4.1, Fig. 7.15). Nonetheless, constraining the model as well as the uncertainty in the ground truth values are severe limitations. The ActiveAx model, when is applied to the same data, yields estimate of axonal diameter far outside of a range predicted by histology, $d_{est} = 7.3\,\mu m$ (Sec. 7.3.1).

Relevant characteristics of the diffusion spectra can be predicted by a small number of structural properties of the trajectories (Eq. 6.10, Eq. 6.11, Fig. 7.6). These properties do not describe well-defined aspects of the trajectories, such as their amplitude and wavelengths, but rather parameters such as microscopic orientation dispersion μOD and a dispersion-weighted wavelength $\lambda_\sigma$ (Sec. 4.4.3).

The Axonal trajectory model could represent also axons with diameter below $d < 4\,\mu m$, which can be found in the corpus callosum. Recent work suggests that the resolution limit of the estimation of axonal diameter using clinical scanners is around $d \approx 4\,\mu m$ meaning that for any axonal diameter below $d < 4\,\mu m$ the estimate $d = 0\,\mu m$ is equally good [54].

It is not claimed the Axonal trajectory model is the correct model of the brain white matter. Axonal trajectory model rather serves as a toy-example that – with a similar approach and similar degree of uncertainty in its assumptions - criticizes current state-of-the-art model that estimates axonal diameter, ActiveAx. The thesis shows that there exists an alternative model that uses, as a source of contrast, different axonal properties, produces results that are more congruent with histology, explores the consequences of different the constraints more openly, and can explain some of its pitfalls.

Non-straight axonal trajectories need to be considered in the modeling of axons (Sec. 7.3.1). In the previous works, axonal trajectories were omitted, i.e. modeled as straight wires [16, 18]. The inspection of the assumptions of diffusion spectra associated with cylinders and axonal trajectories demonstrated that the diffusion spectra are similar for low enough frequencies (Fig. 7.9). Restricting the gradient waveforms to probe only low frequencies (i.e. long diffusion times) yield a relatively high goodness quality of fit (Fig. 7.11). The goodness of fit is often misinterpreted as the degree of correspondence between the model and reality. Models need to be invariant to the experimental setup.

Complex geometries of the intra-axonal space that also include stochastic features need to be considered in the modelling of brain white matter. The estimated parameters of stochastic axonal trajectories may substantially differ from harmonic axonal trajectories although they both map onto the same signal value. In the literature, often only

stochasticity in the extra-axonal space is considered [14].

The forward model of the axonal trajectories was formulated only for 2 out of 3 parameters: $D_\infty$, $\omega$ but not for p. Formulating the forward model for the power behavior at low frequencies p may enable further identification of a subclass of axonal trajectories corresponding to a single diffusion spectrum. The values of p differed for corresponding harmonic axonal trajectories and stochastic axonal trajectories differed (Tab. 7.1, Tab. 7.2) which suggests that further sub-classification might be possible.

In the parallel direction, the Axonal trajectory model assumes that the axons do not exhibit time-dependent diffusion and can be modeled by a simple tortuosity model: $D_{\parallel;\mathrm{ic}} = D_{0;\mathrm{ic}} \cdot \gamma$. However, from the theoretical analysis of the thesis (Sec. 4.4.3) follows that the time-dependent behavior is expected, and it is also measured in-vivo [55].

Studies that investigate the properties axonal trajectories in corpus callosum systematically were not found. The microscopical images used to estimate the wavelength and amplitudes of axonal undulations may be misleading. Before the tissue is examined, the native biological sample needs to be processed but it is distorted during the process. To illustrate the complexity of the processing the steps that are taken are listed: the sample is fixated to preserve it and prevent from the decay, processed to remove water, embedded into a solid block, sectioned into very thin slices and stained to enhance the variations of colors or shades [56].

The Axonal trajectory model assumes that the extra-axonal compartment can be modeled by a free diffusion with the diffusion coefficient given by $D_{\mathrm{ec}} = D_0 \cdot \gamma$, where $\gamma \leq 1$ is a tortuosity limit. Recent works indicate that it may not be the case, the diffusivity of the extra-axonal space may be frequency dependent [57] and the overall signal even dominated by the extra-axonal time-dependent diffusion [14].

The Axonal trajectory model assumes that the intra- and extra-axonal space is impermeable due to myelin layer. However, in conditions associated with demyelination such assumption may not hold and exchange of water molecules may be prevalent [58, 59]. If the model was applied in similar conditions, it may need to be modified.

We do not exclude that there may exist different models of non-straight axons, e.g. 3-dimensional, that could yield results that could match more closely with measured data [60]. However, even such 3-D models may need to include, often omitted, the detailed structure of axons [20].

# Chapter 9

# Conclusions

1. The time-dependence of diffusion in a 1D-toy model of axonal trajectories can be investigated by its associated diffusion spectra. Within the proposed model the axonal trajectories can be classified as harmonic and stochastic.

2. We found that the resulting spectra were characterized by a phenomenological model incorporating three parameters. These three parameters were related to statistical descriptors of the trajectories, namely microscopic orientation dispersion and dispersion-weighted wavelength.

3. Incorporating trajectory-parameters in the model of white matter diffusion yielded fit residuals as small as those obtained with current state-of-the-art models assuming parallel, straight, and cylindrical cylinders. However, the cylinder model predicted axon diameters far outside the range expected from histology. The effect can be explained from the perspective of time-dependent diffusion.

4. When applied to state-of-the-art data acquired in human brain white matter of a healthy volunteer, we found that it was not possible to estimate all three parameters, but by constraining two of them to plausible values we could estimate the third that was within the range predicted by histology.

5. Under the assumption that the axonal trajectories can be modeled by the proposed 1D-toy model and their associated diffusion spectra it is not possible to estimate the exact pathways of axonal trajectories but only their associated statistical descriptors.

6. The estimated parameters of axonal trajectories were congruent with the values predicted by histology. We conclude that neglecting the axonal trajectories leads to biased models of axons in brain white matter.

# Chapter 10

# Outlook

The results demonstrate that plausible values of axonal trajectories can be obtained from the data. However, inverting the forward problem poses a major challenge and additional model assumptions have been made. Congruence between the estimated values and the predicted values obtained from histology may be only a coincidence.

Further validation is necessary. It would be useful to verify the concept on a pre-clinical scanner. The pre-clinical scanners can probe larger range of frequencies due to the absence of safety limitations and different hardware. It may be useful to use oscillating gradient waveforms that could be more sensitive to the high-frequency part of the diffusion spectra [61]. It may be useful to optimize gradient waveforms to facilitate to solution of the inverse problem [22]. In-vivo evaluation on a phantom that mimics the axonal trajectories is advisable. The model should be also predictive in different parts of the nervous system, both in central (e.g. optic nerve) as well as in the peripheral nervous system (e.g. phrenic nerve).

To overcome the flaws of the current dMRI methods, three following general rules can be employed. Firstly, to encode more information (or less information depending on an application) into the dMRI signal and to accurately find out which information is encoded. Secondly, to perform an advanced modeling that connects the measured signal to the underlying tissue parameters but also estimates the degree to which is the proposed parameters are confounded by other parameters. And, lastly, perform well-designed in-vivo experiments, both on clinical and pre-clinical MRI scanners, that are specifically designed to probe the limits and disprove the proposed methods.

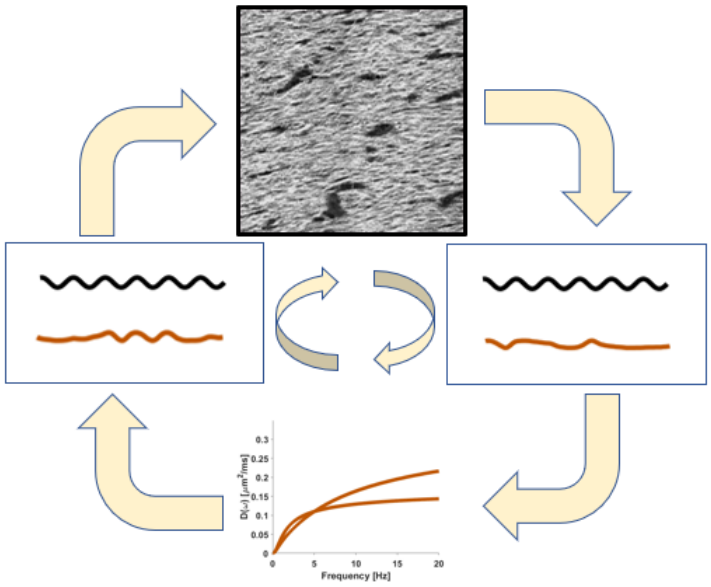

Figure 10.1: **Aims of the thesis.** A model of axonal trajectories based on microscopical images was proposed and investigated from the point of time-dependent diffusion. The parameters of axonal trajectories were estimated from the diffusion magnetic resonance signal and compared to the predicted values from microscopical images.

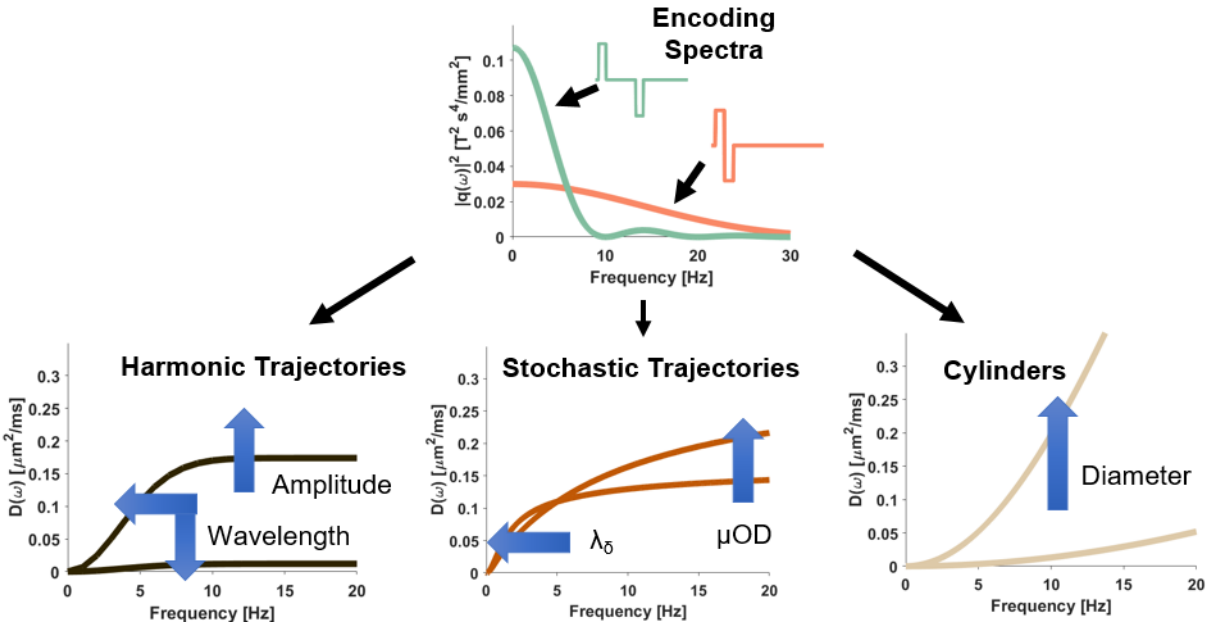


Figure 10.2: **How to design an experiment.** When using gradients that probe long diffusion times, observable differences, being the inner product between encoding and diffusion spectra, becomes almost indistinguishable between cylinders, stochastic and harmonic trajectories. Probing the whole spectrum of diffusion times may provide contrast to distinguish between various types of geometries.

# Appendix

## Publication of results

The results were/will be published at two conferences.

First was submitted and accepted as oral presentation at the European Society for Magnetic Resonance in Medicine and Biology (*ESMRMB 2017*) conference that was held in Barcelona during October 19 - 21, 2017. The abstract was published in the conference proceedings: *Springer Berlin Heidelberg; Magnetic Resonance Materials in Physics, Biology and Medicine; Volume 30; Issue 1 Supplement, October 2017; Book of Abstracts ESMRMB 2017 (e-only); ISSN: 1352-8661; ESMRMB 2017, 34th Annual Scientific Meeting, Barcelona, ES, October 19 – October 21: Abstracts, Saturday.*

Second was submitted to the joint conference of International Society for Magnetic Resonance in Medicine and ESMRMB (*ISMRM - ESMRMB 2018*). The acceptance is not known at the time of publishing the master thesis.

## Implementation of results

A *Monte Carlo simulator* was implemented in MATLAB environment. It was used to compute diffusion spectra of harmonic axonal trajectories by computation of instantaneous velocities and instantaneous displacements, signal by the phase accrual and signal from encoding and diffusion spectra.

A *Gaussian Sampling method* was implemented in MATLAB environment. It was used to generate and characterize stochastic axonal trajectories and compute their diffusion spectra.

Implementation of *analytical predictions* of restricted simple geometries was implemented in MATLAB environment.

## Derivation of diffusion spectra

### Free diffusion (1D)

Knowledge of the velocity of freely diffusing particles is not predictive in other particles. The motion is uncorrelated:

$$\langle \mathrm{v}(0)\mathrm{v}(\mathrm{t})\rangle = \left\{ \begin{array}{ll} \mathrm{v}^2(\mathrm{t}) = \frac{\Delta \mathrm{x}^2(\mathrm{t})}{\Delta \mathrm{t}} & , \text{for } \mathrm{t} = 0 \\ 0 & , \text{for } \mathrm{t} > 0 \end{array} \right\} = \mathrm{D}(0)\delta(\mathrm{t}) = \mathrm{D}\delta(\mathrm{t})$$

The diffusion spectrum is a line:

$$\mathrm{D}(\omega) = \mathrm{D} \tag{10.1}$$

Since the Fourier transform of a delta function $\delta(\mathrm{t}) = 1$.

## Restricted diffusion in simple geometries (1D, 2D, 3D)

Diffusion spectra of the inner compartments of planar (1D), cylindrical (2D) and spherical (3D) restricted geometries are given by the sum of Lorentzians [21, 39]:

$$\mathrm{D}(\omega) \ = \mathrm{D}_0 \sum_{\mathrm{k}=1}^{\infty} \frac{\mathrm{a_k B_k} \omega^2}{\mathrm{a_k^2 D_0^2} + \omega^2} \tag{10.2}$$

where $\mathrm{D}_0 = \mathrm{D}_{\mathrm{t}\to\infty}$ is the bulk diffusivity, $\mathrm{a_k}$ and $\mathrm{B_k}$ are coefficients depending on the geometry, given by:

$$\mathrm{a_k} = \left(\frac{\zeta_\mathrm{k}}{\mathrm{R}}\right)^2 \tag{10.3}$$

$$\mathrm{B_k} = \frac{2(\mathrm{R}/\zeta_\mathrm{k})}{{\zeta_\mathrm{k}}^2 + 1 - \mathrm{d}} \tag{10.4}$$

Where $\zeta_\mathrm{k}$ are the kernels of the:

$$\zeta \mathrm{J}_{\mathrm{d}/2-1}(\zeta) - (\mathrm{d}-1)\mathrm{J}_{\mathrm{d}/2}(\zeta) = 0 \tag{10.5}$$

and $\mathrm{J}_\nu$ denotes the $\nu$-th order Bessel function of the first kind, $\mathrm{d} = 1$, 2 or 3 for planar, cylindrical or spherical restrictions, respectively. 2R is the diameter of the restricted compartment size. For low enough frequencies $\omega \to 0$ the functional dependence of the diffusion spectra $\mathrm{D}(\omega)$ is: $\mathrm{D}(\omega \to 0) \to \omega^2$.

# Acknowledgments

I am sincerely grateful to my main supervisor, Markus Nilsson, for inspiration, substantial support and encouragement. To Jan Pallon, the thesis co-supervisor, and to Samo Lasič for great discussions and editing. To Björn for navigation and help, to Filip, for support and being (not only) the figure guru. To my family, especially to my parents, for their relentless support even situations when I am not a perfect child. To Jane, Marie and Bob for language editing and superb hosting back in the good old days. And to the whole of MR physics group in Lund.

# Bibliography


[1] Moseley, M. *et al.* Diffusion-weighted mr imaging of acute stroke: correlation with t2-weighted and magnetic susceptibility-enhanced mr imaging in cats. *American Journal of Neuroradiology* **11**, 423–429 (1990).

[2] Moseley, M. *et al.* Early detection of regional cerebral ischemia in cats: comparison of diffusion-and t2-weighted mri and spectroscopy. *Magnetic resonance in medicine* **14**, 330–346 (1990).

[3] Basser, P. J., Mattiello, J. & LeBihan, D. Mr diffusion tensor spectroscopy and imaging. *Biophysical journal* **66**, 259–267 (1994).

[4] Mori, S., Crain, B. J., Chacko, V. P. & Van Zijl, P. Three-dimensional tracking of axonal projections in the brain by magnetic resonance imaging. *Annals of neurology* **45**, 265–269 (1999).

[5] Potgieser, A. R. *et al.* The role of diffusion tensor imaging in brain tumor surgery: a review of the literature. *Clinical neurology and neurosurgery* **124**, 51–58 (2014).

[6] Schultz, T. Visualization of a dti measurement of a human brain (2017). URL `https://commons.wikimedia.org/w/index.php?title=File:DTI-sagittal-fibers.jpg&oldid=262732269`.

[7] Jones, D. K., Knösche, T. R. & Turner, R. White matter integrity, fiber count, and other fallacies: the do's and don'ts of diffusion mri. *Neuroimage* **73**, 239–254 (2013).

[8] Alexander, A. L., Lee, J. E., Lazar, M. & Field, A. S. Diffusion tensor imaging of the brain. *Neurotherapeutics* **4**, 316–329 (2007).

[9] Pierpaoli, C., Jezzard, P., Basser, P. J., Barnett, A. & Di Chiro, G. Diffusion tensor mr imaging of the human brain. *Radiology* **201**, 637–648 (1996).

[10] Maier-Hein, K. H. *et al.* The challenge of mapping the human connectome based on diffusion tractography. *Nature communications* **8**, 1349 (2017).

[11] Assaf, Y., Freidlin, R. Z., Rohde, G. K. & Basser, P. J. New modeling and experimental framework to characterize hindered and restricted water diffusion in brain white matter. *Magnetic Resonance in Medicine* **52**, 965–978 (2004).

[12] Assaf, Y., Blumenfeld-Katzir, T., Yovel, Y. & Basser, P. J. Axcaliber: a method for measuring axon diameter distribution from diffusion mri. *Magnetic resonance in medicine* **59**, 1347–1354 (2008).

[13] Barazany, D., Basser, P. J. & Assaf, Y. In vivo measurement of axon diameter distribution in the corpus callosum of rat brain. *Brain* **132**, 1210–1220 (2009).

[14] Lee, H.-H., Fieremans, E. & Novikov, D. S. What dominates the time dependence of diffusion transverse to axons: Intra-or extra-axonal water? *arXiv preprint arXiv:1707.09426* (2017).

[15] Horn, A., Ostwald, D., Reisert, M. & Blankenburg, F. The structural–functional connectome and the default mode network of the human brain. *Neuroimage* **102**, 142–151 (2014).

[16] Alexander, D. C. *et al.* Orientationally invariant indices of axon diameter and density from diffusion mri. *Neuroimage* **52**, 1374–1389 (2010).

[17] Dyrby, T. B., Burke, M., Alexander, D. & Ptito, M. Undulating and crossing axons in the corpus callosum may explain overstimation of axon diameters with activeax. In *Joint Annual Meeting ISMRM-ESMRMB 2014*.

[18] Nilsson, M., Lätt, J., Ståhlberg, F., Westen, D. & Hagslätt, H. The importance of axonal undulation in diffusion mr measurements: a monte carlo simulation study. *NMR in Biomedicine* **25**, 795–805 (2012).

[19] Wang, T., Zhang, H., Hall, M. & Alexander, D. The influence of macroscopic and microscopic fibre orientation dispersion on diffusion mr measurements: A monte-carlo simulation study.

[20] Marco, P., Clemence, L., Edwin, H.-G. & Julien, V. Can we detect the effect of spines and leaflets on the diffusion of brain intracellular metabolites? *NeuroImage* (2017).

[21] Stepišnik, J. Time-dependent self-diffusion by nmr spin-echo. *Physica B: Condensed Matter* **183**, 343–350 (1993).

[22] Westin, C.-F. *et al.* Q-space trajectory imaging for multidimensional diffusion mri of the human brain. *Neuroimage* **135**, 345–362 (2016).

[23] Brown, R. W., Haacke, E. M., Cheng, Y.-C. N., Thompson, M. R. & Venkatesan, R. *Magnetic resonance imaging: physical principles and sequence design* (John Wiley & Sons, 2014).

[24] Hanson, L. G. Introduction to magnetic resonance imaging techniques (2009).

[25] Hanson, L. G. Is quantum mechanics necessary for understanding magnetic resonance? *Concepts in Magnetic Resonance Part A* **32**, 329–340 (2008).

[26] Hoult, D. The origins and present status of the radio wave controversy in nmr. *Concepts in Magnetic Resonance Part A* **34**, 193–216 (2009).

[27] Topgaard, D. Multidimensional diffusion mri. *Journal of Magnetic Resonance* **275**, 98–113 (2017).

[28] Basser, P. J. & Pierpaoli, C. Microstructural and physiological features of tissues elucidated by quantitative-diffusion-tensor mri. *Journal of magnetic resonance* **213**, 560–570 (2011).

[29] Evans, L. *Partial Differential Equations* (American Mathematical Society, 1998). URL `https://books.google.se/books?id=5Pv4LVB_m8AC`.

[30] Einstein, A. Über die von der molekularkinetischen theorie der wärme geforderte bewegung von in ruhenden flüssigkeiten suspendierten teilchen. *Annalen der physik* **322**, 549–560 (1905).

[31] Callaghan, P. T. *Translational dynamics and magnetic resonance: principles of pulsed gradient spin echo NMR* (Oxford University Press, 2011).

[32] Price, W. S. Pulsed-field gradient nuclear magnetic resonance as a tool for studying translational diffusion: Part 1. basic theory. *Concepts in Magnetic Resonance Part A* **9**, 299–336 (1997).

[33] White, N. S. *et al.* Diffusion-weighted imaging in cancer: physical foundations and applications of restriction spectrum imaging. *Cancer research* **74**, 4638–4652 (2014).

[34] Novikov, D. S. & Kiselev, V. G. Effective medium theory of a diffusion-weighted signal. *NMR in Biomedicine* **23**, 682–697 (2010).

[35] Novikov, D. S., Jespersen, S. N., Kiselev, V. G. & Fieremans, E. Quantifying brain microstructure with diffusion mri: Theory and parameter estimation. *arXiv preprint arXiv:1612.02059* (2016).

[36] Shemesh, N. *et al.* Conventions and nomenclature for double diffusion encoding nmr and mri. *Magnetic resonance in medicine* **75**, 82–87 (2016).

[37] Stejskal, E. O. & Tanner, J. E. Spin diffusion measurements: spin echoes in the presence of a time-dependent field gradient. *The journal of chemical physics* **42**, 288–292 (1965).

[38] Dunn, P. F. *Measurement and data analysis for engineering and science* (CRC press, 2014).

[39] Lasič, S., Åslund, I. & Topgaard, D. Spectral characterization of diffusion with chemical shift resolution: highly concentrated water-in-oil emulsion. *Journal of Magnetic Resonance* **199**, 166–172 (2009).

[40] Jeffery, G. Pns features of rodent optic nerve axons. *Journal of Comparative Neurology* **366**, 370–378 (1996).

[41] Mikula, S., Binding, J. & Denk, W. Staining and embedding the whole mouse brain for electron microscopy. *Nature methods* **9**, 1198–1201 (2012).

[42] Lontis, E. R., Nielsen, K. & Struijk, J. J. In vitro magnetic stimulation of pig phrenic nerve with transverse and longitudinal induced electric fields: analysis of the stimulation site. *IEEE Transactions on Biomedical Engineering* **56**, 500–512 (2009).

[43] Jonas, J. B., Müller-Bergh, J., Schlötzer-Schrehardt, U. & Naumann, G. Histomorphometry of the human optic nerve. *Investigative ophthalmology & visual science* **31**, 736–744 (1990).

[44] Fleischhauer, K. & Wartenberg, H. Elektronenmikroskopische untersuchungen über das wachstum der nervenfasern und über das auftreten von markscheiden im corpus callosum der katze. *Cell and Tissue Research* **83**, 568–581 (1967).

[45] Aboitiz, F., Scheibel, A. B., Fisher, R. S. & Zaidel, E. Fiber composition of the human corpus callosum. *Brain research* **598**, 143–153 (1992).

[46] Liewald, D., Miller, R., Logothetis, N., Wagner, H.-J. & Schüz, A. Distribution of axon diameters in cortical white matter: an electron-microscopic study on three human brains and a macaque. *Biological cybernetics* **108**, 541–557 (2014).

[47] Zemmoura, I. *et al.* How klingler's dissection permits exploration of brain structural connectivity? an electron microscopy study of human white matter. *Brain Structure and Function* **221**, 2477–2486 (2016).

[48] Mangin, J.-M. & Gallo, V. The curious case of ng2 cells: transient trend or game changer? *ASN neuro* **3**, AN20110001 (2011).

[49] Johnson, V. E., Stewart, W. & Smith, D. H. Axonal pathology in traumatic brain injury. *Experimental neurology* **246**, 35–43 (2013).

[50] Takagi, T. *et al.* Visualization of peripheral nerve degeneration and regeneration: monitoring with diffusion tensor tractography. *Neuroimage* **44**, 884–892 (2009).

[51] Alexander, D. C., Dyrby, T. B., Nilsson, M. & Zhang, H. Imaging brain microstructure with diffusion mri: Practicality and applications. *NMR in Biomedicine* (2017).

[52] Alexander, D. C. Modelling, fitting and sampling in diffusion mri. *Visualization and processing of tensor fields* 3–20 (2009).

[53] Ferizi, U. *et al.* Diffusion mri microstructure models with in vivo human brain connectome data: results from a multi-group comparison. *NMR in Biomedicine* **30** (2017).

[54] Nilsson, M., Lasič, S., Drobnjak, I., Topgaard, D. & Westin, C. Resolution limit of cylinder diameter estimation by diffusion mri: The impact of gradient waveform and orientation dispersion. *NMR in Biomedicine* (2017).

[55] Fieremans, E. *et al.* In vivo observation and biophysical interpretation of time-dependent diffusion in human white matter. *NeuroImage* **129**, 414–427 (2016).

[56] Mescher, A. L. *Junqueira's Basic Histology: Text and Atlas.* Basic Histology (McGraw-Hill Education / Medical, 2015), 14th edn.

[57] Lam, W. W., Jbabdi, S. & Miller, K. L. A model for extra-axonal diffusion spectra with frequency-dependent restriction. *Magnetic resonance in medicine* **73**, 2306–2320 (2015).

[58] Nilsson, M., van Westen, D., Ståhlberg, F., Sundgren, P. C. & Lätt, J. The role of tissue microstructure and water exchange in biophysical modelling of diffusion in white matter. *Magnetic Resonance Materials in Physics, Biology and Medicine* **26**, 345–370 (2013).

[59] Nilsson, M. *et al.* On the effects of a varied diffusion time in vivo: is the diffusion in white matter restricted? *Magnetic resonance imaging* **27**, 176–187 (2009).

[60] Ferizi, U. *et al.* A ranking of diffusion mri compartment models with in vivo human brain data. *Magnetic resonance in medicine* **72**, 1785–1792 (2014).

[61] Does, M. D., Parsons, E. C. & Gore, J. C. Oscillating gradient measurements of water diffusion in normal and globally ischemic rat brain. *Magnetic resonance in medicine* **49**, 206–215 (2003).